Eur. Phys. J. Appl. Phys. **32**, 73–93 (2005)
DOI: 10.1051/epjap:2005082

THE EUROPEAN PHYSICAL JOURNAL
APPLIED PHYSICS

Scattering of low coherence radiation and applications

G. Popescu[1] and A. Dogariu[2,a]

[1] G.R. Harrison Spectroscopy Laboratory, Massachusetts Institute of Technology, Cambridge, MA 02139, USA
[2] College of Optics and Photonics, University of Central Florida, Orlando, FL 32816, USA

Received: 30 March 2005 / Received in final form: 12 September 2005 / Accepted: 6 October 2005
Published online: 13 December 2005 – © EDP Sciences

Abstract. In an effort to understand complex scattering phenomena, characteristics of optical waves such as polarization, angular spectrum, and temporal coherence have been extensively studied. In this article we will review several applications where the coherence properties of broad-band radiation offer unique sensing and diagnostic capabilities.

PACS. 42.25.-p Wave optics – 42.25.Kb Coherence – 42.25.Dd Wave propagation in random media – 42.25.Hz Interference

1 Introduction

Phenomena related to light propagation in optically inhomogeneous media are being studied for many purposes. Amongst them, the medical applications occupy a special place, since it has been proven that scattering of optical radiation can be used as a noninvasive investigation tool. Remarkable advances in fundamental understanding and experimental methodologies proved that techniques based on multiple light scattering offer unprecedented capabilities in different areas of material sciences.

Due to characteristics such as beam directionality and intensity, the use of highly coherent radiation produced by lasers has been the undisputed choice for many light scattering procedures. Recent developments in light sources and detection techniques offer new, more sophisticated experimental possibilities. For instance, the use of radiation with adjustable spatial and temporal coherence properties determines scattering regimes which can be uniquely related to the structure of a scattering system.

In this article we will review some recent developments in using broadband (low-coherence) radiation for evaluating different characteristics of scattering media of practical interest. We will show how, by adjusting the coherence properties of light, one can use interferometric approaches to select specific orders of scattering and we will illustrate these capabilities in several applications. We will discuss aspects related to both the direct scattering and the inverse problem where the specific interaction is used to infer structural properties in static and dynamic systems, in weakly and strongly scattering media.

[a] e-mail: adogariu@mail.ucf.edu

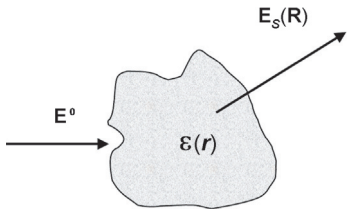

Fig. 1. Electromagnetic field scattering on a dielectric structure.

2 Scattering of low-coherence radiation

We will start by reviewing the phenomenology associated with optical scattering. A typical experiment is illustrated in Figure 1 where a plane wave $\mathbf{E}^0$ with the wave vector $k = \omega/c$ is incident on a spatially random medium occupying a finite volume V. Light is scattered by local inhomogeneities of the dielectric constant $\varepsilon(\mathbf{r})$ and the basic theory provides the link between the experimentally accessible intensity $I_s(\mathbf{R}) = |\mathbf{E}_s(\mathbf{R})|^2$ and the microscopic structure of the random medium.

The starting point of the scattering theory is to describe the total electric field $\mathbf{E}(\mathbf{r})$ as a summation of the incoming and scattered fields and to consider that it satisfies $\left(\nabla^2 + k^2\right)\mathbf{E}(\mathbf{r}) = -4\pi \mathsf{V}(\mathbf{r})\,\mathbf{E}(\mathbf{r})$, where $\mathsf{V}(\mathbf{r})$ represents a generic scattering potential. This equation can be converted into an integral form and, for $\mathbf{R}$ sufficiently far from the scattering volume, one eventually obtains the general result [1,2]

$$\mathbf{E}_s(\mathbf{R}) = \frac{e^{ikR}}{R}\frac{k^2}{4\pi} \times \int_{(V)} d\mathbf{r}\left\{-\mathbf{k}_s \times \left[\mathbf{k}_s \times (\varepsilon(\mathbf{r}) - 1)\cdot \mathbf{E}(\mathbf{r})\right]\right\} e^{-i\mathbf{k}_s\cdot\mathbf{r}}, \quad (1)$$

Article published by EDP Sciences and available at http://www.edpsciences.org/epjap or http://dx.doi.org/10.1051/epjap:2005082

where $\mathbf{k}_s$ is the scattering vector. This expression represents the scattered field as an outgoing spherical wave that depends on the direction and magnitude of the total field inside the scattering volume V.

Approximate solutions can be obtained for the case of weak fluctuations of the dielectric constant. One can expand the field $\mathbf{E}(\mathbf{r}) = \mathbf{E}^0(\mathbf{r}) + \mathbf{E}_1(\mathbf{r}) + \mathbf{E}_2(\mathbf{r}) + ...$ in terms of increasing orders of the scattering potential and use successive approximations of $\mathbf{E}(\mathbf{r})$ in equation (1) to obtain the so-called Born series. In the spirit of a first iteration, one replaces $\mathbf{E}(\mathbf{r})$ with $\mathbf{E}^0(\mathbf{r})$ and obtains the first Born approximation that describes the regime of single scattering.

Alternatively, one can write $\mathbf{E}(\mathbf{r}) = \exp[\Psi(\mathbf{r})]$ and develop the series solution for $\Psi(\mathbf{r})$ in terms of increasing orders of the scattering potential. This is the Rytov's series of exponential approximations, an alternative to the algebraic series representation of the Born method. The two approaches are almost equivalent; however, preference is sometimes given to Rytov's method because an exponential representation is believed to be more appropriate to describe waves in line-of-sight propagation problems [3–5].

It is worth pointing out here that equation (1) can be regarded as an integral equation for the total field and, because the total field is a superposition of the incident field and contributions originating from scattering from all volume V, this generic equation includes all possible multiple scattering effects [2,6].

2.1 Weakly scattering media

2.1.1 Structure and form functions

When a sparse distribution of scattering centers is contained in the volume V, all the scattering centers are practically exposed only to the incident field, $\mathbf{E}(\mathbf{r}) = \mathbf{E}^0(\mathbf{r}) = E^0\mathbf{e}^0 e^{i\mathbf{k}\cdot\mathbf{r}}$ where E^0 is the field magnitude, $\mathbf{e}^0$ is the polarization direction, and $\mathbf{k}$ is the wave vector. A considerable simplification is introduced when the magnitude of the scattered field is much smaller than that of the incident field, such that the total field inside the medium can be everywhere approximated with the incident field. This is the condition of the first Born approximation for tenuous media that practically neglects multiple scattering effects inside the scattering volume V. From equation (1), it follows that

$$\mathbf{E}_s(\mathbf{R}) = E^0 \frac{e^{ikR}}{R}\frac{k^2}{4\pi} \times \int_{(V)} d\mathbf{r}\ \left[\mathbf{e}^s \cdot (\varepsilon(\mathbf{r}) - 1)\cdot \mathbf{e}^0\right]\ e^{-i\mathbf{k}_s\cdot\mathbf{r}}. \quad (2)$$

For instance, in the case of a system of N identical particles, equation (2) is evaluated to give

$$\mathbf{E}_s(\mathbf{R}) = E^0 \frac{e^{ikR}}{R}\frac{k^2}{4\pi}\sum_{j=1}^{N} e^{-i\mathbf{k}_s\cdot\mathbf{r}_j} \times \int_{(V_j)} d\mathbf{r}\ \left[\mathbf{e}^s \cdot (\varepsilon(\mathbf{r}) - 1)\cdot \mathbf{e}^0\right]\ e^{-i\mathbf{k}_s\cdot\mathbf{r}}, \quad (3)$$

where V_j is the volume of the j-th particle located at $\mathbf{r}_j$. In terms of the scattering wave vector $\mathbf{q} = \mathbf{k}_s - \mathbf{k}$, the integral in equation (3) has the meaning of the single-scattering amplitude of the j-th particle, $F(\mathbf{q}) = |f|\cdot B(\mathbf{q})$, and depends on the forward scattering amplitude f and a scattering amplitude normalized such that $B(0) = 1$. The ratio between the refractive index of the particles n_p and of the suspending medium n_s determines the scattering strength f of an individual scatterer while its shape and size are accounted for in $B(\mathbf{q})$.

For a collection of discrete scattering centers, the total scattered intensity of equation (3) factorizes like [7]

$$I(\mathbf{q}) = \left(E_i \frac{e^{ikR}}{R}\frac{k^2}{4\pi}\right)^2 N\ F^2(\mathbf{q}) \times \sum_{i,j=1}^{N} e^{-i\mathbf{q}\cdot(\mathbf{r}_i - \mathbf{r}_j)} \sim NP(\mathbf{q})\,S(\mathbf{q}), \quad (4)$$

where we separated the single-scattering form factor $P(\mathbf{q})$ from the interference function or the static structure factor $S(\mathbf{q}) = \sum_{i,j=1}^{N} e^{-i\mathbf{q}\cdot(\mathbf{r}_i - \mathbf{r}_j)}$. The structure factor quantifies the phase-dependent contributions due to different locations of scattering centers. When an ensemble average is taken over the volume V and after separating out the diagonal terms, the static structure factor can be written as [7,8]

$$S(\mathbf{q}) = 1 + \left\langle e^{-i\mathbf{q}\cdot(\mathbf{r}_i - \mathbf{r}_j)}\right\rangle = 1 + \rho\int G(\mathbf{r})\, e^{-i\mathbf{q}\cdot\mathbf{r}} d\mathbf{r} \quad (5)$$

in terms of the pair-correlation function $G(\mathbf{r})$ (where $\mathbf{r}$ is the distance between two particles) describing the statistical properties of the spatial arrangement of scattering centers. It is through $S(\mathbf{q})$ that the link is made between the statistical mechanics description of the inhomogeneities and the measurable quantities in a scattering experiment.

As can be seen from equation (5), for the case of particles separated by distances much larger than the wavelength, $S(\mathbf{q})$ becomes unity; the situation corresponds to $G(\mathbf{r}) \equiv 1$, i.e. constant probability to find scattering centers anywhere in the scattering volume. This regime characterized by $S(\mathbf{q}) = 1$ is also called the incoherent case of volume scattering where $I(\mathbf{q})$ is a simple, intensity-based summation of individual contributions originating from different scattering centers.

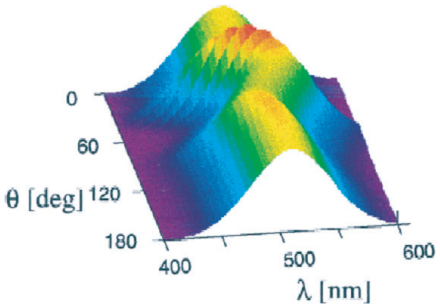

Fig. 2. Spectrum of the scattered light in the far field at different angles of scattering, calculated for monodispersed systems of spherical particles with radius $a = 150$ nm and volume fraction 45%. The spectrum of the incident field has a Gaussian shape with 70 nm $FWHM$, centered at $\lambda = 500$ nm.

2.1.2 Spectral changes due to spatial correlations

When radiation with spectral density $\Re^{(0)}(\omega)$ is incident on a generic scattering potential, the far-field spectrum of the scattered radiation is determined by both the incident field and the spatial correlation of the scattering potential and depends on both the incident and scattering directions

$$\Re(\mathbf{q},\omega) = \frac{1}{r^2}\widetilde{F}(-\mathbf{q},\omega)\, W^{(0)}(\omega), \tag{6}$$

where $\widetilde{F}$ represents the Fourier transform of the two-point correlation function of the scattering potential. For a review of correlation-induced spectral changes see reference [9].

Using equation (4), one immediately infers that in the case of discrete random media, the far-field spectrum becomes [10]

$$\Re(\mathbf{q},\omega) = \frac{V}{r^2} S(\mathbf{q}-\mathbf{q}_0) \left|\widetilde{F}(\mathbf{q},\omega)\right|^2 \Re^{(0)}(\omega). \tag{7}$$

To illustrate this effect, Figure 2 presents the spectrum of the scattered light in the far field at different angles of scattering, calculated for a monodisperse system of spherical particles with radius 150 nm and a volume fraction 45%. The spectrum of the incident field has a Gaussian shape with 70-nm FWHM, and it is centered at $\lambda = 500$ nm.

2.2 Strong scattering

So far, we introduced the basic description of the single scattering process, which applies to sparse distributions of particles. For the single scattering regime to be applicable, the average dimension of the scattering medium must be smaller than the mean free path l_s. However, in many situations this is not the case and the light travels through the medium over distances much longer than l_s and encounters many scattering events during the propagation. In this case, the simple treatment presented earlier does not apply and the complexity of the problem is significantly increased. A full vector solution to the field propagation

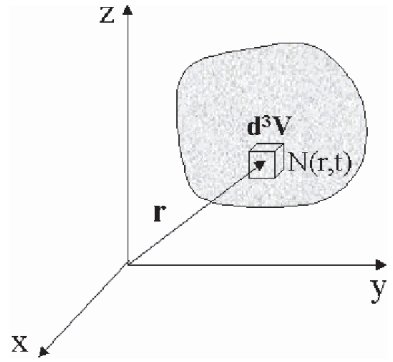

Fig. 3. Scattering medium under transport conditions.

in dense media is not yet available and even for scalar theories, analytical results can only be found for special, limiting cases of multiple scattering regimes.

2.2.1 Radiative transport equation

The transport description in the case of a highly scattering medium is based on a photon random walk picture which is similar to that used in other areas of physics, such as solid state physics and nuclear reactor physics [11]. The wave correlations that may survive this heavy scattering regime are completely neglected, while each individual scattering event is considered an independent process.

Using the energy (photon) conservation principle, the final goal of the transport theory is to find the time-dependent photon distribution at each point in the scattering medium.

In order to write the transport equation, we first identify all the contributions that affect the photon balance within a specific volume V, as depicted in Figure 3. Thus, we obtain the following transport equation in its integral form:

$$\left\{\int_V \frac{dn}{dt} + v\mathbf{\Omega}\nabla n + v\mu n(\mathbf{r},\mathbf{\Omega},t) - \int_{4\pi}\left[v'\mu_s(\mathbf{\Omega}'\to\mathbf{\Omega})\, n(\mathbf{r},\mathbf{\Omega}',t)\right] d\mathbf{\Omega}' - s(\mathbf{r},\mathbf{\Omega},t)\right\} d^3r\, d\mathbf{\Omega} = 0. \tag{8}$$

In the equation above, n is the photon density, while μ and μ_s are the total and scattering coefficient, respectively. The first term denotes the rate of change in the energy density, the second term represents the total leakage out of the boundary, the third term is the loss due to scattering, the fourth term accounts for the photons that are scattered into the direction $\mathbf{\Omega}$, while the last term represents the possible source of photons inside the volume. Using the fact that the volume V was arbitrarily chosen, the integral of equation (8) is identically zero if and only if the integrand vanishes. Thus, the differential form of the

transport equation is obtained as:

$$\frac{dn}{dt} + v\mathbf{\Omega}\nabla n + v\mu n(\mathbf{r},\mathbf{\Omega},t) - \int_{4\pi} [v'\mu_s(\mathbf{\Omega}' \to \mathbf{\Omega})n(r,\mathbf{\Omega}',t)]\, d\mathbf{\Omega}' - s(\mathbf{r},\mathbf{\Omega},t) = 0. \quad (9)$$

The same equation can be expressed in terms of the angular flux $\varphi(\mathbf{r},\mathbf{\Omega},t) = v \cdot n(\mathbf{r},\mathbf{\Omega},t)$:

$$\frac{1}{v}\frac{d\varphi}{dt} + \mathbf{\Omega}\nabla\varphi + \mu\varphi(\mathbf{r},\mathbf{\Omega},t) - \int_{4\pi} [\mu_s(\mathbf{\Omega}' \to \mathbf{\Omega})\varphi(\mathbf{r},\mathbf{\Omega}',t)]\, d\mathbf{\Omega}' - s(\mathbf{r},\mathbf{\Omega},t) = 0. \quad (10)$$

The initial condition for this equation is $\varphi(\mathbf{r},\mathbf{\Omega},0) = \varphi_0(\mathbf{r},\mathbf{\Omega})$, while the boundary condition is $\varphi(\mathbf{r}_s,\mathbf{\Omega},t)_{r_s\in S} = 0$, if $\mathbf{\Omega}\mathbf{e}_s < 0$. The transport equation, although just an approximation of the real physical problem, can be solved in most cases only numerically. As we will see in the next section, further simplifications to this equations are capable of providing solutions in closed forms and will, therefore, receive a special attention.

2.2.2 Diffusion approximation of the transport theory

Equation (10) can be integrated with respect to the solid angle Ω, such that the result can be expressed in terms of the photon flux Φ and the current density J as a continuity equation:

$$\frac{1}{v}\frac{d\Phi}{dt} + \nabla\mathbf{J}(\mathbf{r},t) + \mu\Phi(\mathbf{r},t) = \mu_s\Phi(\mathbf{r},t) + s(\mathbf{r},t). \quad (11)$$

As can be seen, equation (11) contains two independent variables Φ and J

$$\Phi(\mathbf{r},t) = \int_{4\pi}\varphi(\mathbf{r},\mathbf{\Omega},t)d\Omega \quad (12)$$
$$J(\mathbf{r},t) = \int_{4\pi}\mathbf{\Omega}\varphi(\mathbf{r},\mathbf{\Omega},t)d\Omega\,,$$

and, therefore, an additional assumption is needed to make the computations tractable. In most cases, one can assume that the angular flux φ is only linearly anisotropic

$$\varphi(\mathbf{r},\mathbf{\Omega},t) \simeq \frac{1}{4\pi}\Phi(\mathbf{r},t) + \frac{3}{4\pi}J(\mathbf{r},t)\cdot\mathbf{\Omega}. \quad (13)$$

The equation above represents the first order Legendre expansion of the angular flux and is the key approximation that allows obtaining the diffusion equation. It is also referred to as the P_1 approximation, since it represents a Legendre polynomial P_l, for $l = 1$. In addition, the photon source is considered to be isotropic and the photon current to vary slowly with time: $(1/|\mathbf{J}|)(\partial\mathbf{J}/\partial t) << v\mu_t$. Under these conditions, the equation that relates $\mathbf{J}$ and Φ can be derived, which is known as the Fick's law

$$J(\mathbf{r},t) = -\frac{1}{3\mu_t}\cdot\nabla\Phi(\mathbf{r},t) = -D(r)\nabla\Phi(\mathbf{r},t). \quad (14)$$

In the equation above, $\mu_t = \mu - g\mu_s$ is the transport coefficient. The parameter g represents the anisotropy factor, i.e. the average cosine of the scattering angle which is defined in terms of elementary solid angles before and after scattering as $g = \langle\mathbf{\Omega}\cdot\mathbf{\Omega}'\rangle$. The parameter g accounts for the fact that, for large particles, the scattering pattern is not isotropic. In equation (14), $D(r)$ is the diffusion coefficient of photons in the medium and is the only parameter that contains information about the scattering medium. At this point, combining equations (11, 14), one obtains the diffusion equation, which has been extensively used in solving scattering problems

$$\frac{1}{v}\frac{\partial\Phi}{\partial t} - \nabla\left[D(r)\nabla\Phi(\mathbf{r},t)\right] + \mu_a(\mathbf{r})\Phi(\mathbf{r},t) = S(\mathbf{r},t). \quad (15)$$

In the equation above, μ_a represents the absorption coefficient and $S(\mathbf{r},t)$ is the photon source considered to be isotropic. Note that the diffusion equation breaks down for short times of evolution, i.e. for $t < l_t/c$. In other words, it takes a finite amount of time for the diffusion regime to establish. Although restricted to a particular situation of multiple light scattering, the diffusion treatment finds important applications in practice. The diffusion description of waves propagating in random media will be extensively used in the next chapters.

Using appropriate boundary conditions, equation (15) can be solved for particular geometries. Once the photon flux Φ is calculated, the current density J can be obtained using Fick's law [11]. The current density $J(r,t)$ is the measurable quantity in a scattering experiment and thus deserves special attention. The total optical power measured by a detector is proportional with the integral of $J(r,t)$ over the area of detection. The temporal variable t represents the time of flight for a photon between the moment of emission and that of detection. When a constant group velocity is assumed, this variable can be transformed into an equivalent one- the optical pathlength, $s = vt$. Thus, the path-length probability density $P(s) = J(s)/\int_0^\infty J(s)ds$, i.e. the probability that the photons traveled within the sample an equivalent optical pathlength in the interval $(s,\ s+ds)$, can also be evaluated. The path-length distribution $P(s)$ is the central quantity in evaluating various statistical averages describing the regime of strong multiple scattering.

3 Low-coherence interferometry techniques

Interference is the fundamental phenomenon by which electromagnetic fields interact with one another. Interferometric methods have found important applications in investigating a wide range of phenomena, from the nature of

light itself to spectroscopy and material characterization. Let us consider a given complex field as a superposition of field components

$$\mathbf{E}(\mathbf{r},t) = \sum_i \mathbf{E}_i(\mathbf{r},t). \tag{16}$$

The intensity of the total field, which is the measurable quantity, is thus the time average of the modulus squared associated with the total complex amplitude, $I(\mathbf{r},t) = \left\langle |\mathbf{E}(\mathbf{r},t)|^2 \right\rangle$. For only two interfering fields, the result simplifies to

$$I(\mathbf{r},t) = \left\langle |\mathbf{E}_1|^2 \right\rangle + \left\langle |\mathbf{E}_2|^2 \right\rangle + \langle |\mathbf{E}_1 \cdot \mathbf{E}_2^*| \rangle + \langle |\mathbf{E}_1^* \cdot \mathbf{E}_2| \rangle \,, \tag{17}$$

where I_1 and I_2 are the intensities of the two fields. For monochromatic fields of parallel polarizations and identical optical frequencies, the intensity of the interference is

$$I(\mathbf{r},\tau) = |E_1|^2 + |E_2|^2 + 2\,|E_1|\,|E_2| \cos\left[\Delta\phi(\mathbf{r},\tau)\right], \tag{18}$$

where $\Delta\phi$ is the phase difference between the two fields.

The interference term in equation (18) is particularly relevant for practical applications. If for instance, one field is frequency shifted with respect to the other, such that the phase of the interference term becomes $\Delta\phi = \Delta\omega\tau + \delta\phi$, the interference term will be oscillating at a selected frequency permitting high-fidelity measurements. Since the measured signal is proportional to the product of two fields, one of which can be used as an amplifier, very low-amplitude fields can be detected. Additionally, because the interference term depends only on the squared root of each intensity, interferometric measurements allow for high dynamic range measurements.

Recent developments in the light source technology allowed generation of broad spectrum light with high power levels, which become suitable for scattering experiments. Such sources with broad band spectra include light emitting diodes (LED), superluminescent diodes (SLD), and femtosecond laser sources. The electric field associated with a polychromatic radiation

$$E(\omega, r) = E_0(\omega) \cdot e^{-i\cdot(\omega t - kr)} \tag{19}$$

has a spectral density (optical spectrum)

$$S(\omega) = \langle E_0(\omega) \cdot E_0(\omega)^* \rangle \,, \tag{20}$$

where the angular brackets stand for ensemble average and * for complex conjugation. Typically, an optical spectrum is characterized by its bandwidth $\Delta\omega$, conventionally defined as the full width half maximum and a central frequency ω_0. A particular class of broad-band light is the so called *quasi-monochromatic* radiation for which $\Delta\omega/\omega_0 \ll 1$. This condition is equivalent to requiring that the envelope of a short pulse (or of the autocorrelation function for continuous wave) varies much slower in time than the oscillations of the central frequency (carrier). This situation is also known as the *slowly varying envelope approximation*, commonly used for describing various processes of light matter interaction. The low-coherence radiation used in the following chapters can be considered as quasi-monochromatic light.

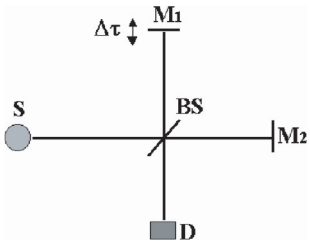

Fig. 4. Michelson interferometry with partially coherent light.

The fundamental difference in nature between monochromatic and polychromatic radiation appears most clearly in the regime of multiple scattering. The multiple scattering of coherent light creates a complicated distribution of maxima and minima with a very sharp intensity contrast, known as *speckles*. This distribution is a signature of the medium and can be used to characterize its structure. In similar conditions of scattering, low-coherence light will generate a distribution of maxima and minima with much lower contrast, i.e. a smeared speckle pattern. This phenomenon, can be easily explained by recognizing that a distribution of speckles is nothing more than a complicated fringe pattern generated by the superposition of waves that traveled in the medium over different trajectories, accumulating different optical phases. While in the case of coherent light, waves with arbitrary phase distributions produce interference, the maximum phase difference between interfering *low-coherence* waves is limited by the coherence length of the radiation.

The creation of speckles is a rather well understood phenomenon. Its fundamental principle of interference uncovers the main difference in nature between monochromatic and polychromatic light. The lack of interference can be beneficial when one tries to suppress multiple scattering. It is precisely the interference phenomenon that isolates the specifics of low-coherence versus monochromatic light in specific applications dealing with media characterization. The example of speckles has shown already that, in the multiple scattering regime, the limited temporal coherence acts as a band pass filter in the optical path-length domain suppressing the multiple scattering component from the interfering signal. This is the underlaying principle for the optical techniques described in the following.

3.1 Michelson interferometry

Let us consider that the light beam emerging from a source S is divided into two beams by a beam splitter BS, as illustrated in Figure 4. The two beams are reflected by the mirrors M_1 and M_2 and subsequently recombined at the detector D. Considering that the time delay between the two beams is $\Delta\tau$, the condition to obtain interference fringes can be simply stated as

$$\Delta\tau \cdot \Delta\omega \leq 1, \tag{21}$$

where $\Delta\omega$ is the bandwidth of light. In order to describe the interference phenomenon, let us introduce the real electric field in its Fourier representation [12]:

$$E^{(r)}(r,t) = \int_{-\infty}^{+\infty} E(r,\omega)\cdot\exp(-i\omega t)d\omega. \tag{22}$$

An important property of the real signal $E^{(r)}(r,t)$ is that its Fourier pair $E(r,\omega)$ is a Hermitian function, i.e. $E(r,-\omega) = E^*(r,\omega)$, meaning that the negative frequency components ($\omega < 0$) do not provide any information which is not already contained in the positive ones ($\omega > 0$). Thus, the so-called complex analytic signal associated with $E^{(r)}(r,t)$ can be employed

$$E(r,t) = \int_{0}^{+\infty} \breve{E}(r,\omega)\cdot\exp(-i\omega t)d\omega. \tag{23}$$

This means that, in the absence of negative frequency components, each Cartesian component of E, considered as a function of complex variable t, will be analytic and regular in the lower half of the complex t-plane. From equations (22, 23), it follows that

$$E(r,t) = \frac{1}{2}\left[E^{(r)}(r,t) + iE^{(i)}(r,t)\right], \tag{24}$$

where the real and imaginary parts of E form a Hilbert pair

$$E^{(i)}(r,t) = \frac{P}{\pi}\int_{-\infty}^{+\infty}\frac{E^{(r)}(r,t')}{t'-t}dt' \tag{25}$$

$$E^{(r)}(r,t) = -\frac{P}{\pi}\int_{-\infty}^{+\infty}\frac{E^{(i)}(r,t')}{t'-t}dt'.$$

In equation (25), P denotes the Cauchy principal value.

From now on, the spatial variable will be dropped, i.e. we will consider that $r = r_1 = r_2$, since in the experimental geometries of interest here the fields are spatially coherent and overlapped at the detector. We also assumed that the interfering fields are stationary. In the conditions of the Michelson interferometer depicted in Figure 4, the total electric field at the detector D is

$$E(t) = E_1(t) + E_2(t+\tau). \tag{26}$$

The detected intensity is evaluated as a ensemble average over the realizations of the total field and takes the form:

$$I = \langle E(t)\cdot E^*(t)\rangle, \tag{27}$$

where * denotes the complex conjugation. It follows from equations (26, 27) that

$$I(\tau) = I_1 + I_2 + 2\,\mathrm{Re}\left[\Gamma(\tau)\right] \tag{28}$$

where

$$\Gamma(\tau) = \langle E_1(t)\cdot E_2^*(t+\tau)\rangle. \tag{29}$$

When the fields on the two arms are identical, the function $\Gamma(\tau)$ is known as the field autocorrelation function. The normalized degree of coherence, $\gamma(\tau) = \Gamma(\tau)/\Gamma(0)$, is a measure of the sharpness of the interference fringes; it takes values between zero and unity which are associated with completely decorrelated and fully coherent fields, respectively. The dependence of γ on τ measures the spread in the time delay over which the interference can be observed. As we will discuss in the next sections, for specific applications, a very narrow interference pattern is desired, corresponding to distance delays in the range of several microns. A basic theorem of stochastic processes, called the Wiener-Khintchine theorem, states that the power spectrum (spectral density) $\Re(\omega)$ of the random process and its autocorrelation function $\Gamma(\tau)$ form a Fourier transform pair [12]:

$$\Gamma(\tau) = \int_{0}^{\infty}\Re(\omega)\exp(-i\omega\tau)d\omega \tag{30}$$

$$\Re(\omega) = \int_{-\infty}^{\infty}\Gamma(\tau)\exp(i\omega\tau)d\tau.$$

In equation (30), $\Re(\omega)$ represents the spectrum of light at the detector and the Wiener-Khintchine theorem asserts that it can be fully reconstructed from the field autocorrelation function Γ.

Low-coherence interferometry provides certain practical advantages as compared with interferometric techniques involving laser radiation. It is apparent from equation (30) that there is a reciprocal relationship between the spectral composition of an optical field and its coherence properties. Thus, measuring one property, offers experimental access to the other.

Fourier transform infrared (FTIR) spectroscopy is one important interferometric application, where spectral information is obtained by measuring the cross-correlation function of two fields interfering in a Michelson geometry. Various related techniques have been developed during the past years (for a review, see [13] and references therein). FTIR spectroscopy has been established as a standard technique for measuring the infrared absorption and emission spectra of most materials, with substantial advantages in signal-to-noise ratio, resolution, speed, and detection limits. Practically, all compounds show characteristic absorption/emission in the IR and, thus, can be analyzed efficiently by FTIR.

A broad optical spectrum implies a short coherence time, as suggested by equation (30). Thus, LCI is suitable for optical gating applications. Optical time-domain reflectometry (OTDR) uses this principle for measuring depth-resolved reflectance [14]. This technique has found important applications especially in characterizing the location and the magnitude of losses due to scattering within waveguide media, sites which were previously inaccessible for measurement.

Optical coherence tomography (OCT) has been developed as an extension of OTDR for biological tissue investigation [15]. In OCT, the end result consists of a set of cross correlations between a reference wave and the field scattered from biological tissue. In this case, the short coherence length of the field allows mapping the tissue under investigation in terms of its scattering properties. Especially due to its integration with optical fibers, OCT has become widely popular and various biomedical diagnostic applications (for a review, see [16]).

In Fourier domain OCT, the mechanical scanning of the reference mirror, which is instrumental in reconstructing the cross-correlation function, is replaced with a single spectrum measurement provided by a spectrometer, as demonstrated with spectral interferometry [17]. This type of measurement can be regarded as the FTIR measurement principle in reverse. However, it has been recently shown that, using a broad spectrum for experiments on scattering media, one has to be careful in interpreting the detected signal, as the detection efficiency is drastically influenced by the spectral content of the field [18].

Spectroscopic OCT is an extension to the traditional method, which provides spatially-resolved spectroscopic information about the biological structure [19]. Phase dispersion and absolute phase measurements have also been proven to have a great potential for investigating transparent biological structures in both static and dynamic conditions [20,21]. More recently, new methods for quantitative phase imaging with both low- and high-coherence fields have been proposed as powerful biological tools for studying structure and dynamics [22–24].

3.2 Sagnac interferometry

As discussed earlier, light scattering from optically inhomogeneous media is in general a complicated phenomenon resulting in different orders of scattering ranging from single to heavily multiple scattering components. Due to the limited coherence length associated with broad band radiation, low-coherence interferometry can be efficiently used to filter out specific components of the scattered light. In the following, we will present an interferometric geometry which is used to suppress the scattered light in a transmission geometry.

Sagnac interferometers rely on overlapping two counter-propagating beams as opposed to Michelson type geometries where the two interfering fields propagate along different physical paths. The experimental setup is depicted in Figure 5 and can be described as a Sagnac-Michelson interferometer, as it combines both a counter-propagating geometry and a separate reference field. A broadband source emits light with a central wavelength of 1.33 μm and a FWHM bandwidth of 60 nm [25].

The light is coupled into a single-mode optical fiber that enters the 2×2 fiber coupler FC1 and, on the probe arm, the beam is divided once more by the 1×2 fiber coupler FC2. The power delivered in the coupler FC2 is about 60 μW. The two fiber ends are connected to the collimators C1 and C2, which are aligned such that they send the parallel beams in counter-propagating directions, as in a Sagnac interferometer. The main components of the electric field reaching the detector are

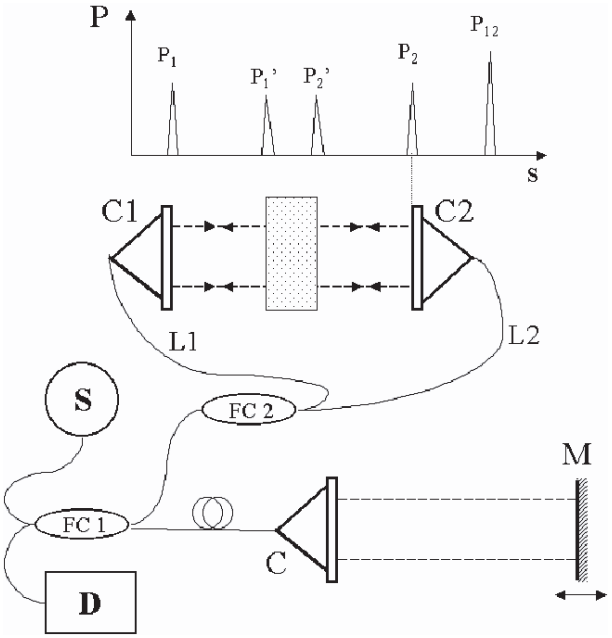

Fig. 5. Experimental setup: S source, FC's fiber couplers, C's collimaters, M mirror, s the path-length delay due to the scanning mirror, D detector. The interference peaks correspond to different interfaces, as indicated.

$$E_D(t) = E_0(t)e^{iks} + E_{11}(t)e^{ikL_{11}} + E_{12}(t)e^{ikL_{12}} + E_{21}(t)e^{ikL_{21}} + E_{22}(t)e^{ikL_{22}}, \quad (31)$$

where E_{11} and E_{22} correspond to the paths that involve reflections on $C1$ and $C2$, respectively, while E_{12} represents the field emitted through $C1$ and coupled by $C2$, and E_{21} is the time-reversed counterpart of E_{12}. In equation (31), k is the wave vector, L_{ij}, $i, j = 1, 2$, are the optical path-lengths associated with the fields E_{ij}, and s is the optical path-length traveled on the reference arm. Using equation (31), the expression for the irradiance at the detector, as a function of the optical path-length set by the reference mirror, takes the form

$$I_D(s) = I_0 + \sum_{i,j}^{1,2} I_{ij} \left|\gamma[k(s - L_{ij})]\right| \cos[k(s - L_{ij})] \quad (32)$$

where I_{ij} is the amplitude of the interference term between the field E_{ij} and the reference, while γ is the complex degree of coherence associated with the source. This equation determines the position of the interference peaks as the mirror M sweeps the reference arm. The positions of the interference peaks are denoted in Figure 5.

Since $\bar{L_{12}} = \bar{L_{21}}$, the peaks associated with I_{12} and I_{21} are spatially overlapped. In this configuration, the fiber lengths differ by about 2.5 cm and, therefore, P_1 and P_2

appear at different positions. When an object with reflecting boundaries is inserted between $C1$ and $C2$, two additional dielectric interfaces are present and two peaks will appear accordingly, denoted in Figure 5 by P_1' and P_2', thus both the position of the object and its thickness can be measured with an accuracy limited only by the coherence length. If the object is transparent, the shift in the position of P_{12} will measure the optical path-length of the object. We will show in the following that this specific geometry is quite efficient in suppressing the undesired scattered light and isolating accurately the ballistic components in dense scattering media.

3.2.1 Measurement of ballistic attenuation

The customary description of the attenuation suffered by a monochromatic light beam propagating in a scattering, non-absorbing medium is given by the Lambert-Beer law: $P = P_0 \exp(-L/l_s)$, where P_0 is the initial power, P is the remaining power after traveling a distance L, while l_s is the scattering mean free path that characterizes the inhomogeneous medium. When absorption is present, there a similar exponential decay, but the decay rate is replaced by $1/l_s + 1/l_a$, with l_a the absorption length. Deviations from the Lambert-Beer law due to multiple scattering have been quantified [26] and corrections have been proposed [27]. Various techniques for filtering out the scattered light have been explored, including heterodyne detection [29], confocal spatial filtering [28] temporal gating [30–32], and polarization filtering [33]. Modifications of classical Lambert-Beer dependence of light attenuation have also been observed in the case of highly-correlated scattering systems [34].

We will describe here how LCI can be used for measuring this ballistic component. When a scattering medium is placed between $C1$ and $C2$, the magnitude of the peak P_{12} describes quantitatively the beam attenuation due to the scattering process. Using the heterodyne detection, one can evaluate this attenuation over a dynamic range of more than 80 dB and the short coherence length of the light offers the temporal selectivity necessary to isolate the early-arriving ballistic waves. Figure 6 illustrates the transmission results for different scattering media consisting of suspensions of particle (0.121 μm, 0.356 μm, and 3.135 μm, in diameter) for which the scattering cross-sections, σ_s, are 9.78×10^{-14} cm^2, 5.0×10^{-11} cm^2, and 2.83×10^{-7} cm^2, respectively. As it can be seen, the experimental decay sharply ends at the noise level of the device, indicating that the filtering of scattered light is virtually complete due to both the coherence and angular gating. However, a disagreement can be observed between the experimental data and the expectation of the Lambert-Beer law, denoted by dashed lines in Figure 6. One should also notice that the deviation from the negative exponential behavior becomes more important for samples of smaller particle size. This particle size dependence of the ballistic light attenuation is unexpected and an interpretation more refined than the conventional Lambert-Beer law is needed. As opposed to the monochromatic case described

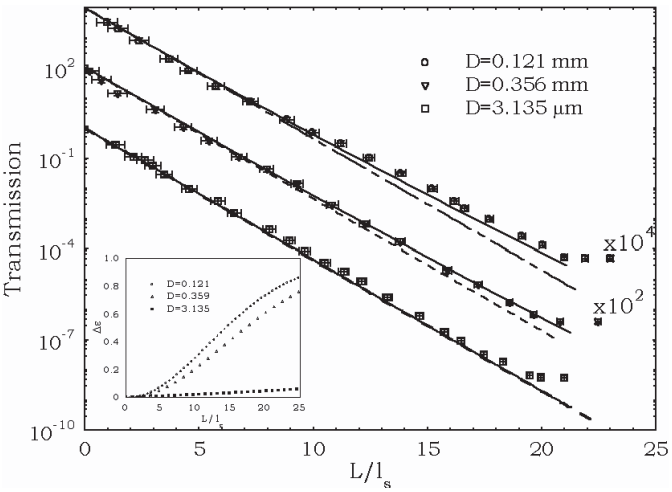

Fig. 6. Ballistic attenuation for suspensions of different particle sizes. The data is scaled as indicated; the dashed lines represent negative exponentials, while the solid lines are given by the convolution model. The inset shows the relative difference between the transmission given by the model and that of Lambert-Beer law as a function of optical thickness L/l_s.

by the Lambert-Beer law, the spectral density in our measurements approaches a Gaussian with a FWHM of about 60 nm, centered at $\lambda_0 = 1.33$ μm. In this case, the transmission coefficient, defined as the ratio between the transmitted and the incident power, takes the form:

$$T_{\Delta\lambda}(\lambda_0) = \int_{-\infty}^{+\infty} S_{\Delta\lambda}(\lambda - \lambda_0) \exp\left[-N\sigma_s(\lambda)L\right] d\lambda. \quad (33)$$

Equation (33) asserts that the overall transmitted light is given by the summation of the contributions from all the frequency components, weighted by the initial optical spectrum and it takes the form of a convolution between the Lambert-Beer transmission and the incident spectral density $S_{\Delta\lambda}(\lambda - \lambda_0)$, of central frequency λ_0 and width $\Delta\lambda$. It can be easily seen in Figure 6 that the dependence of equation (33), which is indicated by continuous lines, describes much better the experimental results for all the particle sizes. As shown in the inset of Figure 6, where the relative difference $\Delta\varepsilon = (T_{\Delta\lambda} - T_0)/T_0$, with T_0 being the Lambert-Beer transmission function, is plotted as a function of optical density, the correction brought to the Lambert-Beer law by equation (33) has an increasing importance as the particle size decreases and becomes negligible for large particles. The reason is that the scattering cross-section depends stronger on the size parameter $2\pi R/\lambda$, for smaller values of the particle radius R. Therefore, in this range of size parameters, the particles are characterized by different scattering cross sections corresponding to each frequency component of the optical spectrum. For large particle sizes, the cross sections associated with individual spectral components do not change significantly over the incident spectrum and, thus, the overall attenuation approaches the negative exponential decay, as in the case of monochromatic light.

It is worth mentioning that time-gated measurements can also provide the path-length selectivity necessary to isolate the ballistic light component [30]. However, the heterodyne detection provides a considerable dynamic range; the decay of the ballistically transmitted light is limited only by the noise level of the device and not by the diffusive component of light. One should also be aware of the fact that the dynamic range available in our particular experiments does not represent a fundamental limit of the interferometer performance being still far from the shot-noise limit [30]. We found that, due to the broad spectrum, the ballistic transmission behavior data deviates from the Lambert-Beer law with an increasing amount for smaller scatterers. This is explained by considering that the propagating light is a superposition of monochromatic components, which attenuate at different rates. It should be noted that the quantitative analysis in low-coherence imaging techniques relies heavily on the validity of conventional Lambert-Beer attenuation for light propagating toward and scattering back from a target surrounded by a turbid medium. The technique described here should find applications for characterization of random media as well as for medical and biological investigation.

The ability to efficiently suppress the multiple scattering light suggested that the present geometry can be used to investigate the sedimentation process of highly dense colloidal particles. This particular application will be presented in the next section, in the context of retrieving the size distribution of particles in dense colloidal suspensions.

3.2.2 Measurement of particle sedimentation

The Sagnac-Michelson interferometric technique presented earlier is filtering efficiently the scattered light from the ballistic component transmitted through a dense scattering medium. The beam is collimated and passes through the sample parallel to the liquid surface, at a distance h below this plane, as shown in Figure 7. The detector monitors the transmission of light through the sample as it evolves in time. For a heterogeneous distribution of particle sizes, the transmission has the Lambert-Beer form

$$T = \exp\left(-L\sum_i N_i\sigma_i\right), \tag{34}$$

where L is the thickness of the sample, N_i and σ_i are the concentration and scattering cross section of the class of particles characterized by the radius R_i. Equation (34) is valid provided that the concentration of the suspension is not very high. For a certain period of time, the transmission through the sample has a constant value, as long as at the depth h below the surface the overall concentration of particles is constant. However, after a time t_1 necessary for the largest particles in the suspension to fall the distance h, the transmission will increase, since the class of largest particles is no longer present in the region where the light beam is passing through the sample. Similarly, at a later time t_2, a class of smaller particles depletes the investigated region, such that another increase in the measured transmission is recorded. This process is illustrated in Figure 7 for a three-modal distribution of particles.

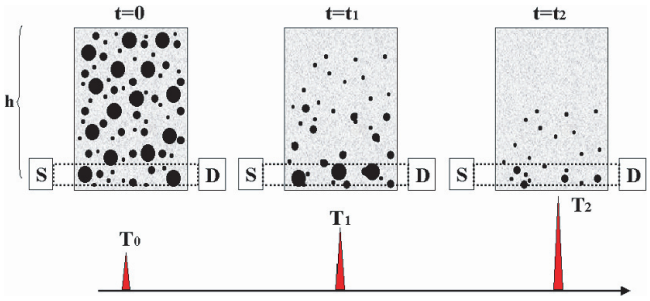

Fig. 7. Sedimentation process in a three-modal suspension.

Since the measurements are taken at discrete times t_k, using equation (34), we relate the transmission at two successive moments by

$$\ln(T_k) = \ln(T_{k-1}) + LN_k\sigma_k \tag{35}$$

where T_k and T_{k-1} are the transmissions measured at the moments t_k and t_{k-1}, respectively, while N_k and σ_k characterize the particles that depleted the region of investigation during the period $\Delta t_k = t_k - t_{k-1}$. Thus, the concentration of these particles can be inferred as

$$N_k = \frac{1}{L\sigma_k}\ln\left[\frac{T_k}{T_{k-1}}\right]. \tag{36}$$

For determining N_k, the only unknown is now σ_k. However, using the Stokes equation, one can calculate the dimension of the particle that traveled the distance h in a time t_k

$$R_k = \left[\frac{9\eta h}{2(\rho_s - \rho_l)g}\cdot\frac{1}{t_k}\right], \tag{37}$$

where η is the viscosity coefficient of the suspending liquid, ρ_s, ρ_l are the densities of the particle and liquid, respectively, and g is the gravitational acceleration. Using the information of refractive index for both the liquid and particles, the cross section σ_k can be calculated from Mie theory at each moment of time. Thus, monitoring the transmission evolution in time, one can infer the sizes of the particles present in the mixture and the particle concentration associated with each size.

It should be noted that no approximations are involved in evaluating the scattering cross sections of the particles. During the measurement, each moment corresponds to a specific class of particle sizes that just exited the beam, which can be evaluated and used further to calculate exactly the corresponding cross section. This can be easily obtained using a simple computer routine. In using this method, no information about initial concentration of particles is needed. Due to the large dynamic range of the detection used, the particle size distribution can be obtained for concentrated suspensions.

This methodology was applied to standard polystyrene suspensions (Duke Scientific) of 3.7 μm having a refractive

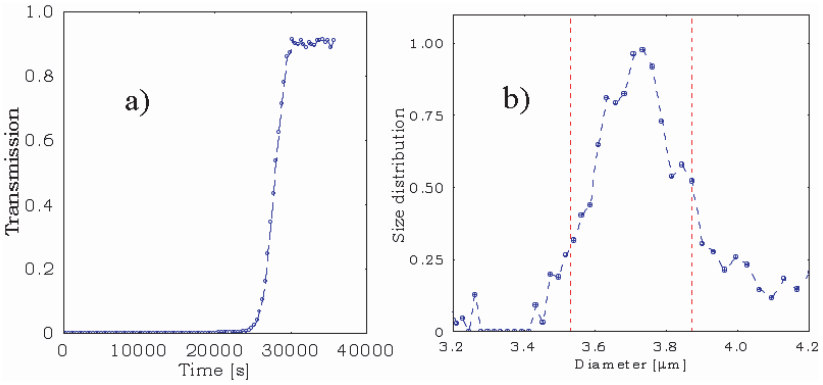

Fig. 8. Time-resolved transmission (a) and particle size distribution (b) inferred, for a suspension of polystyrene particles with the diameter of 3.7 μm. The vertical lines represent the expected size interval provided by the manufacturer.

index of 1.59 and a density of 1.05 relative to water. Figure 8a shows the time evolution of the measured transmission over a period of 10 hours. The sharp jump seen in the experimental curve of Figure 8a suggests that the suspension is highly monodisperse. This is indeed the situation shown by Figure 8b, in which the particle size distribution is reconstructed using the procedure described in earlier. It can be seen that the experimental results on this stabilized suspension agree very well with the specifications provided by the company.

The method is further illustrated in the case of alumina powders of (10.2 ∓ 0.4) μm. A solution was made by mixing the powder with deionized water and the sample has been sonicated for several minutes to limit the aggregation process. Figure 9 shows the experimental results for the time-dependent transmission and particle size distribution. It can be seen that the size distribution is broader than that indicated by the company. There are several possible reasons for this result. First, the finite size of the illuminated beam determines a certain smooting of the resulting size distribution. Second, the suspension created was by no means stabilized, which explains the presence of large particle resulted from agglomeration. The third possible reason is that the particles as provided by the manufacturer are not spherical in shape. The model used assumes spherical particles, for which both the Mie scattering and Stokes velocity models are valid. Therefore, the result obtained with this method is the size distribution of equivalent spherical particles, i.e. characterized by certain hydrodynamic diameters. In many applications, this information is sufficient, since the details of particle shapes are hardly achievable and not critical. To reduce the measurement time for suspensions of small particles one can apply simultaneous centrifugation, which is quite a common procedure for sedimentation investigation.

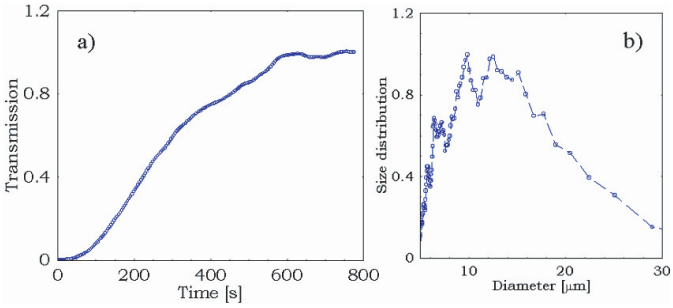

Fig. 9. Time-resolved transmission (a) and particle size distribution (b) inferred, for a suspension of alumina particles with the average diameter of 10.2 μm.

4 Optical pathlength spectroscopy and applications

As discussed in Section 2, the diffusive wave propagation depends on characteristics of the specific scattering geometry and can be characterized by the probability density $P(s)$ of optical pathlengths through the medium. In general, $P(s)$ can be theoretically estimated for different experimental configurations but, so far, direct experimental studies regarding optical pathlengths distribution have been limited to investigations of temporal broadening of short light pulses that propagate diffusively. Based on the LCI principle, we will describe a technique called optical pathlengths spectroscopy (OPS) which infers directly the pathlengths distribution $P(s)$ of waves backscattered from multiple scattering media [35]. From the shape of this distribution, characteristics of the scattering process such as the transport mean free path can be determined.

A typical OPS signal consists of backscattered intensity contributions corresponding to waves scattered along closed loops that have the same optical pathlengths and, in addition, have the total momentum transfer of these waves equal to $4\pi/\lambda$ (backscattering). This is somewhat similar to the information obtained in time-resolved reflectance measurements where the diffusion approximation makes a reasonable description of the experimental data. It should be noted that, as long as the waves propagate with a constant average velocity, even for stationary sources, the waves characterized by the same optical pathlengths, can be considered as being emitted at the same moment. Thus, the pathlengths probability density does not change if a steady-state source is replaced by a short pulse emitted at t_0. In OPS, only the class of waves that have traveled an optical distance which corresponds to the

length of the reference arm is able to produce fringes and is, therefore, detected. In the optical pathlength domain, the interferometer acts as a band-pass filter with a bandwidth given by the coherence length of the source. Accordingly, the shorter the coherence length, the narrower the optical pathlengths interval of backscattered light that will produce detectable fringes. Now, if we let the reference mirror sweep the reference arm, waves with different optical pathlengths through the medium are detected and an optical pathlength distribution is reconstructed. Experimentally, OPS is limited by the fact that the signal corresponding to long paths within the medium is weak and a large dynamic range is needed for accurate measurements of pathlengths distribution tails. However, as opposed to dynamic techniques, the measurements can be extended over longer periods of time and there is no need for sophisticated time-of-flight configurations.

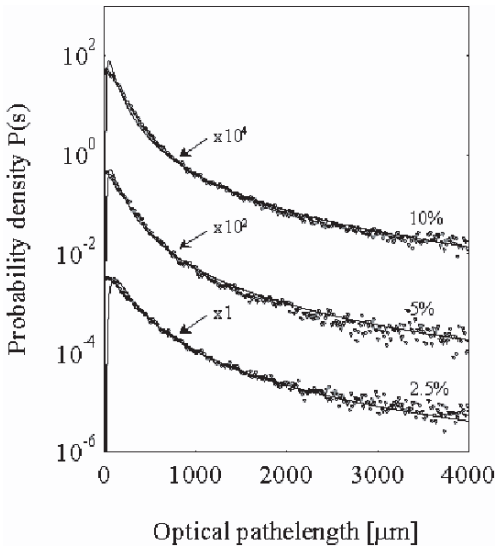

Fig. 10. OPS data for polystyrene suspensions of different concentrations. The curves are scaled as indicated.

4.1 Colloidal systems

In the following, we will illustrate how OPS is used to evaluate to structural characteristics of granular media, liquid and solid systems highly scattering media. An example of OPS signal is shown in Figure 10, where the pathlength-resolved backscattered intensities corresponding to water suspensions of polystyrene microspheres with particle diameter of 0.46 μm and various volume fractions are shown. The values of normalized backscattered intensities have been compared with the corresponding solutions of the diffusion approximation, as described in [35]. In obtaining these results, absorption effects have been neglected because the absorption lengths of the media are roughly two orders of magnitude longer than the corresponding scattering lengths. As can be seen, the diffusion theory makes a good description of the experimental data corresponding to different volume fractions, i.e. different scattering properties. Applying the Mie scattering theory, one can calculate the values of transport mean free paths for the media examined in Figure 10. Excellent agreement is obtained between the Mie-based estimations of l^* and the results obtained by fitting the measurement data within the diffusion approximation. For example, for the samples shown in Figure 10, the measured l^* values of 197, 101, and 49.2 μm are to be compared with, respectively, 206, 103, and 51.5 μm obtained from Mie theory. The error of our l_t measurements was evaluated to be of about 5%. The remarkable agreement proves that reliable measurements of photon transport mean free path can be based on OPS.

4.2 Porous media

Another example of is presented in Figure 11 where OPS is applied to characterize the structure of porous media such as thin membranes (mixtures of cellulose esters, polyvinylidene fluoride and polycarbonate). The membranes consist of interconnected networks of pores which are strong light scatterers with the strength depending on

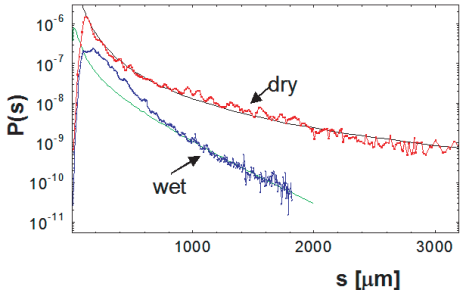

Fig. 11. Optical pathlength distributions in porous media under wet and dry conditions as indicated.

the refractive index contrast and, therefore, on the membrane water content. As can be seen in Figure 11, the presence of water diminishes the refractive index contrast which reduces the scattering ability and leads to shorter average optical pathlength in comparison with the highly scattering (dry) case [36].

The measured OPS signals are well described, at least the tails of the pathlength distributions, by solutions of the diffusion approximation applied to slabs of finite thickness. The results of fitting the measured OPS with the prediction of the diffusion approximation are also shown in Figure 11. Once a reliable structural model is available, the measured pathlength spectra, or just moments of the distribution, can be further used to determine various characteristics related to pore sizes or overall porosity of random media [37]. OPS has been also used to study the diffusion process in bounded media, in particular the influence of the scattering anisotropy on the boundary conditions associated with the diffusion equation [38].

4.3 Dynamic processes

The technique of dynamic light scattering (DLS) has been established as a powerful method for investigating dynamic processes. Measuring the temporal fluctuations of the scattered light, detailed information about the dynamics of the scattering medium can be extracted [39]. Originally, DLS applications were limited to weakly scattering media, where the light propagation could be described by a single-scattering model. An important breakthrough in the field of dynamic light scattering is represented by the extension of DLS to strongly scattering media [40–51]. The technique is referred to as diffusing wave spectroscopy (DWS). In DWS, the intensity of the scattered light is a summation over all the possible scattering trajectories in the medium, while the phase correlations are neglected. Therefore, the coherence length of the radiation used must exceed the longest scattering path detected. If λ is the wavelength of light and N the typical number of scattering events light undergoes in the medium, the characteristic decay time of the temporal autocorrelation function is given by the time it takes for a scatterer to move over a distance of $\lambda/\sqrt{N}$. This characteristic time is much longer in typical DLS experiments, since it is set by the time required by the scatterers to move over a distance of q^{-1}, where q is the wave vector.

The description of the DWS signal relies on a photon diffusion model to obtain the optical pathlength distribution $P(s)$ of waves propagating in the medium. This distribution is usually obtained by assuming a diffusive propagation of optical waves and solving the associated diffusion equation. This technique has been used to study particle motion in concentrated fluids such as colloids, microemulsions, and other systems which are characterized by strong multiple scattering. More recently, important results have been obtained with measurements on viscoelastic fluids [42], magnetorheological suspensions [43], periodically strained suspensions [44], proteins [45], etc. The technique has also been successfully applied to studying non-ergodic systems, such as particles in gel matrix [46].

However, many of the dynamic systems of practical interest, although multiple scattering, are not optically diffusive, and, therefore, cannot be characterized by the DWS treatment presented above. The region of transition from single to diffusive scattering regime, in the context of dynamic light scattering experiments, has been studied and the experimental data have been described using a combination of cumulants weighted by empirical constants [47]. More recently, the theory of DWS was extended using the Poisson photon distribution and numerical solutions to the transport equation [48]. Modeling the light transport with a telegrapher equation and using a discontinuous source model, the technique has been applied to optically thin samples, in a transmission geometry [50]. However, this model is exact only for the one-dimensional case and has limited applicability to describing general, three-dimensional problems of light transport. Thus, so far, dynamic light scattering has found little application for characterizing media which are neither single scattering, nor diffusive. Accordingly, in order to assess accurately the dynamic structure, it is highly desirable to provide a simultaneous and independent measurement of photon pathlength distribution. As we have shown before, $P(s)$ can be obtained experimentally using OPS and, therefore, DWS limits of applicability can be extended to systems which are not optically diffusive.

In quantifying the temporal fluctuations of the light scattered from a dynamic suspension, one has to evaluate the associated field autocorrelation function. For a fluctuating electromagnetic field that scattered multiple times, the normalized autocorrelation function has the form of an average over all possible paths weighted by the optical pathlength probability density [51]:

$$g^{(1)}(\tau) = \int_0^\infty P(s) \exp\left[-\frac{2\tau}{\tau_0}\frac{s}{l_t}\right] ds. \qquad (38)$$

In equation (38), $\tau_0 = (Dk_0)^{-1}$, with D being the diffusion coefficient of the scatterers in the suspending fluid and k_0 the wave vector associated with the optical field. For Brownian particles of diameter d, the diffusion coefficient relates to the temperature T and the viscosity η of the medium through the well known Stokes-Einstein expression $D = k_B T/(3\pi\eta d)$, where k_B is the Boltzmann's constant. In practice, the intensity rather than the field autocorrelation function is measured and, therefore, a relationship between the two autocorrelation functions is always needed.

A typical experimental setup for dynamic scattering measurements is presented in Figure 12 [49]. An Ar^+ laser with the central wavelength of 467 nm is coupled into a single mode fiber which represents one arm of a 1×2 fiber coupler. The output of the coupler is immersed in the colloidal suspension under investigation and the backscattered light is collected through the same fiber. Without additional optical components, the signal is detected by a photomultiplier, connected to a digital correlator. Due to the refractive index contrast between the fiber core and the suspension solvent, the detected signal has two components: the light backscattered from the dynamic system, E_s, and the one due to the Fresnel reflection at the fiber/medium interface, E_F. The total intensity detected can be written as:

$$I(t) = I_s(t) + I_F(t) 2\,\mathrm{Re}\left\{E_s(t)E_F^*(t)\exp[i\Phi(t)]\right\}, \qquad (39)$$

where I_s and I_F are the intensities associated with the scattered and specular component, respectively, while Φ is the phase of the Fresnel reflected field. In our geometry, the specular field is static both in phase and amplitude, thus, neglecting the rapidly varying terms, the intensity autocorrelation function becomes:

$$\begin{aligned} G^{(2)}(\tau) &= \langle I(t)I(t+\tau)^*\rangle \\ &= I_F^2 + 2I_F\langle I_s\rangle + \langle I_s(t)I_s(t+\tau)^*\rangle \\ &\quad + I_F\left[G^{(1)}(\tau) + G^{(1)}(\tau)^*\right]. \end{aligned} \qquad (40)$$

In equation (42), $G^{(1)}$ stands for the autocorrelation function of the scattered field, and the squared brackets for

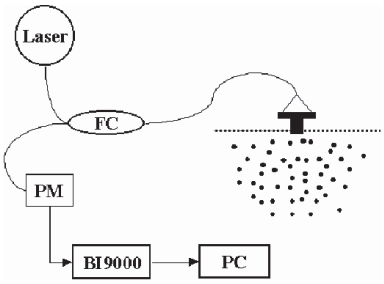

Fig. 12. Experimental set-up for dynamic scattering measurements: FC-fiber coupler, PM-photomultiplier, BI9000-digital correlator, PC-computer.

time averaging. In most practical cases, the Fresnel component is always much stronger than the scattered field and the relationship between the normalized intensity and amplitude autocorrelation functions takes a simple form

$$g^{(2)}(\tau) = 1 + 2\beta \,\mathrm{Re}\left\{g^{(1)}(\tau)\right\}, \qquad (41)$$

where $\beta = \langle I_s \rangle / I_F \ll 1$. Thus, by measuring the intensity autocorrelation function, one can determine the amplitude autocorrelation and obtain information about the dynamic properties of the colloidal suspension through equation (38). The main goal is to use the distribution $P(s)$ measured with OPS, rather than calculating it from a diffusion model. When combining equations (38, 41), both $P(s)$ and $g^{(2)}(\tau)$ are experimentally measured and, therefore, the dynamic properties of the colloid, i.e. τ_0, can be inferred without assuming a diffusive transport of light.

Systematic experiments proved the validity of this approach. Polystyrene microspheres with the diameter of 0.121 μm were suspended in water and their concentration has been adjusted by controlled mixing with deionized water. The dimensions of the samples were the same as in the OPS experiments. However, as the particle concentration is decreasing, the diffusion model is expected to give a less reliable description of the light propagation in these media. Figure 13 shows the pathlength distributions obtained using OPS for suspensions with different values of transport mean free path, as indicated. The solid curves represent the analytic result, corresponding to these transport mean free paths values. As can be seen, the agreement of the experimental data with the diffusion model diminishes considerably as the value of l_t increases. We conclude that for samples of lower concentrations, the diffusion equation does not make a satisfactory description of the optical pathlength distribution. On the other hand, the experimental curves in Figure 13 do not have a simple negative exponential decay meaning that they contain significant multiple scattering features. These scattering media can be characterized as multiple scattering but not yet diffusive; the light scattered by such systems is said to be in a sub-diffusive regime. If, in order to describe the intensity autocorrelation function, one uses equation (38) with $P(s)$ estimated from the diffusion equation, erroneous results are to be expected.

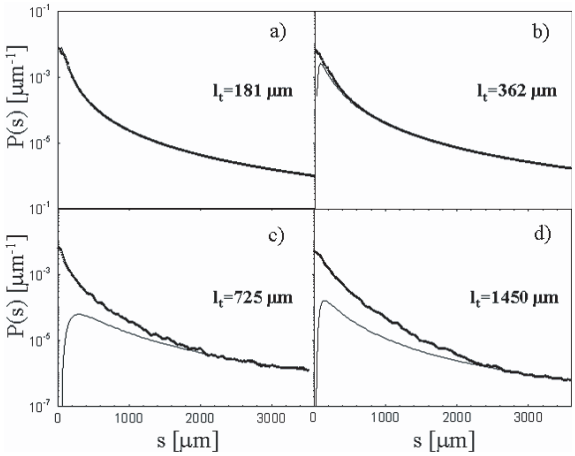

Fig. 13. $P(s)$ measured for suspensions with different values of l_t, as indicated. The continuous lines are obtained from the diffusion model.

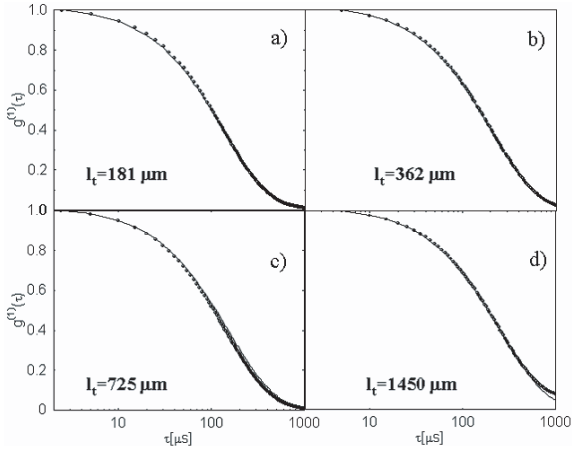

Fig. 14. Normalized field autocorrelation functions for colloidal suspensions of different l_t, as indicated. The continuous lines are the best fit to data obtained by evaluating numerically the Laplace transform of equation (5.1.) with measured $P(s)$ distributions. The dashed lines correspond to the DWS description, as described in text.

In order to overcome this difficulty, one can use the $P(s)$ functions experimentally obtained with OPS, as described earlier. In equation (38), we evaluate numerically the Laplace transform for an interval of values for the characteristic time τ_0. The Laplace transforms are then compared with the data, and the best fit is retained. The results obtained for samples with the same $l_t's$ as those presented in Figure 13 are summarized in Figure 14. The continuous curves are obtained using the procedure outlined here, while the dashed curves are generated by using pathlengths distributions obtained from the diffusion equation, i.e. the conventional DWS treatment. As can be seen, the data is accurately described by our approach for all the samples. Thus, the procedure proposed here can be regarded as a new methodology to obtain the values of τ_0 for any multiple scattering media, without relying on a diffusion model.

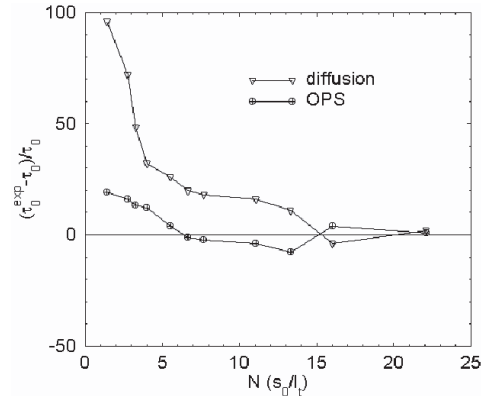

Fig. 15. The relative error of the experimental value $\tau_0^{\exp}$ with respect to the theoretical one τ_0 for a series of colloidal suspensions characterized by different parameters s_m/l_t.

The same approach was applied to systems at various levels of dilution. Of course, the errors introduced by using pathlength distributions given by the diffusion equation are more significant as the transport mean free path increases. The results obtained in terms of the characteristic time associated with colloidal suspensions of same particles over a broader range concentrations, are summarized in Figure 15. For comparison, the results of the best fit obtained using the diffusion model to infer $P(s)$ are also shown on the same graph. The value of $\tau_0 = (Dk_0)^{-1}$ has been calculated for a water viscosity of $\eta = 0.95\,\mathrm{cp}$, corresponding to our working temperature of 22 °C. The plot shows the relative error of the measured $\tau_0^{\exp}$ with respect to the expected value τ_0. The abscissa represents the maximum optical pathlength s_m detected with OPS, normalized to the transport mean free path. In practice, the maximum detectable pathlength is limited by the sensitivity of the detection system and it usually differs from one sample to another.

We would like to point out that, in transmission measurements, the ratio between the thickness of the sample and the transport mean free path is the parameter used to measure the scattering strength of a medium. This ratio is usually referred to as the optical density of the medium. In a backscattering geometry on the other hand, such a geometrical constraint is usually missing, thus, the ratio $N = s_m/l_t$ seems to be the appropriate parameter that can be used instead. From the results summarized in Figure 15, it can be seen that our approach brings a significant improvement over the conventional treatment based on the diffusion model. As the single scattering regime is approached (lower values of N in Fig. 15), the error of our technique increases also, approaching a value of 20%. This is expected, as equation (38) was obtained for $s > l_t$. Nevertheless, our results clearly demonstrate that measuring $P(s)$ experimentally for the particular geometry of the DWS experiments, produces more accurate results than simply using the calculated $P(s)$ distribution. It should be noted that, due to the particular geometry of our measurements, i.e. fiber immersed in suspension, the effects of the anisotropy factor g on the light propagation, which were studied in detail in reference [38], are not likely to be significant. However, if, for other geometries, such subtle corrections are needed, their effect should already be contained in the measured $P(s)$ and no without further data processing is required.

In practice, there are many dynamic systems that multiply scatter light and yet are not optically diffusive. For this class of media, using the technique of DWS, which is based on a diffusion model, inherently gives erroneous results because the pathlength distribution $P(s)$ provided by the diffusion equation fails to describe the light transport in the low-order multiple scattering regime. Using the experimentally determined $P(s)$ permits expanding the use of dynamic light scattering techniques to the intermediate domain of optical densities which is not covered by either DLS or DWS.

5 Dynamic scattering in localized coherence volumes

Due to their flexibility and their extended applicability, many modern experimental geometries of dynamic light scattering involve single-mode optical fibers [52]. Detecting the light with a single-mode optical fiber allows the collection of the fluctuating signal from a spatially coherent area, determined by the properties of the optical waveguide. On the other hand, the temporal coherence of the incident light is known to influence the properties of the dynamic signals in the context of multiple light scattering [53]. Using partially coherent light in an interferometric geometry, Brownian motion of colloidal particles has been investigated in highly scattering media [54]. It is to be expected that tuning the coherence properties of incident radiation could add a new dimension to the scattering process and, therefore, lead to novel investigation techniques for situations which can not be tackled with conventional approaches.

As discussed in the previous section, one of the yet to be solved problems is the scattering from inhomogeneous media that are neither single scattering nor highly diffusive. For a range of practical applications, the scattering regime falls in the transition domain between a low optical density regime, where DLS has been successfully applied for many years, and the regime of high optical density, where DWS approach can give an accurate description. Optical probing of such scattering systems is of considerable interest and in the following section we will describe another approach based on isolating a small scattering volume within a larger multiple scattering medium. The main feature of this approach is that by the intrinsic coherence properties of the broad band light used, the dynamic scattering signal collected is limited to a region comparable in size with the coherence length of the source ($l_c = 30\ \mu$m). Thus, as long as $l_s > l_c$, which holds even for highly scattering media, the data can modelled within the framework of single scattering. This technique has therefore a broad applicability range and also permits spatially-resolved characterization of inhomogeneous systems. The ability to investigate complex fluids will be also addressed.

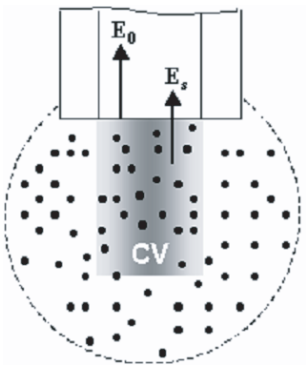

Fig. 16. The coherence volume (CV) determined by the single mode fiber and the properties of the broad-band radiation.

5.1 Measurement of structural properties of highly diffusive materials

Let us start by describing a fiber optics-based technique which permits collecting the backscattered light from a small volume localized at the end of the optical waveguide [25]. A pigtailed super-luminescent diode with a central wavelength of 824 nm and a coherence length of 30 μm is coupled into a single-mode optical fiber, which represents one arm of a 1×2 fiber coupler. The output of the coupler is immersed in the colloidal suspension under investigation and the backscattered light is collected through the same fiber. Without additional optical components, the signal is detected and further analyzed in the frequency domain by a spectrum analyzer. Due to the refractive index contrast between the fiber core and the suspension solvent, the signal detected has two components: the light backscattered from the dynamic system and the one due to the Fresnel reflection at the fiber/medium interface, as shown in Figure 16. The coherence length and the transversal dimension of the fiber core define a coherence volume where the optical fields preserve relative phase correlations. This volume of minute dimensions has a specific relevance for our experiment; the fluctuating scattered light originates in this spatial region only, as will be shown in the following section.

Considering the terms that survive the time averaging, the expression for the intensity auto-correlation function can be derived as

$$G^{(2)}(\tau) = I_0^2 + 2I_0 I_s + {I_s}^2 \tag{42}$$

$$+ I_0 \sum_j I_j \left[g_j(\tau) + g_j(\tau)^*\right] \cdot \exp\left[-2\left(s_j - s_0\right)^2 / l_c^2\right]$$

$$+ \sum_{k \neq l} I_k I_l \cdot g_k(\tau) g_l(\tau)^* \cdot \exp\left[-2\left(s_k - s_l\right)^2 / l_c^2\right].$$

In equation (42), I_0 and $I_s = \sum_j I_j$ are the average intensities of the specular and scattered component, respectively, while I_j is the intensity associated to the backscattered component of trajectory j; g_j represents the normalized first order correlation function corresponding to this component, defined as $g_j(\tau) = \langle E_j(\tau) E_j(t+\tau)^* \rangle / I_j$, with the angular brackets denoting time averaging and the symbol * complex conjugation. The optical path-lengths associated with the scattered component j and the specular field are denoted by s_j and s_0, respectively, while l_c is the coherence length. It is worth mentioning that for the limit of $I_0 = 0$, equation (42) is consistent with the result derived in reference [53], for a self-beating geometry. An important consequence of equation (42) is that, for scattering media with mean free paths longer than $l_c/2$, the backscattered light undergoes in average only one scattering event in the coherence volume, which is defined approximately by the coherence length and the area of the fiber core. Consequently, the auto-correlation functions g_j are independent of the length of the scattering trajectory and are given by the well established formula for the quasi-elastic light scattering. If $I_s \ll I_0$, which is the case in all our experiments, the last (self-beating) term of equation (42) becomes negligible. With these assumptions, equation (42) can be arranged to give the normalized auto-correlation function

$$g^{(2)}(\tau) = 1 + 2\frac{I_0 I_s^{CV}}{\left(I_0 + I_s^{CV}\right)^2} g_1(\tau). \tag{43}$$

In equation (43), $g^{(1)}(\tau) = \exp[-q^2 D\tau]$, with D, the particle diffusion coefficient and q, the scattering vector, which, for our backscattering geometry, equals twice the wave number $(4\pi/\lambda)$. For Brownian particles of diameter d, the diffusion coefficient relates to the temperature T and the viscosity η of the medium through the well known Stokes-Einstein expression $D = k_B T/3\pi\eta d$, where k_B is Boltzmann's constant. The quantity I_s^{CV} that appears in equation (43) represents the average intensity of the light scattered from the coherence volume:

$$I_s^{CV} = \sum_j I_j \exp\left[-2\left(s_j - s_0\right)^2 / l_c^2\right]. \tag{44}$$

For all the real light sources, the coherence length has a finite value and, therefore, the inequality $I_s^{CV} < I_s$ always applies.

In the experiments described here the coherence length is about 30 μm, which means that the investigated media can be optically dense but still analyzed by a single scattering model, as described in equation (43). The fluctuations of the scattered light have been analyzed in the frequency domain, based on the Fourier transform relationship between the intensity auto-correlation function $G^{(2)}(\tau)$ and the power spectrum $P(\omega)$. The associated power spectrum has a Lorentzian shape [39]

$$P(\omega) = \frac{A_0}{\Omega} \cdot \frac{1}{1 + (\omega/\Omega)^2}, \tag{45}$$

where $\Omega = Dq^2$ and A_0 is the spectrum amplitude, proportional with the product $I_0 I_s^{CV}$. Thus, the amplitude A_0 of the power spectrum cis simply $A_0 = \alpha\rho Q_b/d$, where d is the diameter of the particle, Q_b is the backscattering efficiency, ρ is the density of particles by volume, while α is

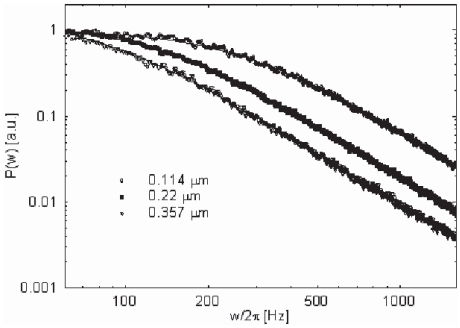

Fig. 17. Power spectra associated with suspensions of particles with different diameters, as indicated. The continuous lines represent the fit with the theoretical description.

an experimental constant. Since the dimension of the particle can be determined from the width of the power spectrum, as described earlier, the backscattering efficiency Q_b can be calculated for particles with known optical properties. Consequently, the particle concentration is obtained by simply measuring the amplitude A_0 and calibrating for the experimental constant α.

Both the line width Ω and the amplitude A_0 of the measured power spectra were accurately determined by fitting the data with equation (45). Typical power spectra fitted with the Lorentzian functional dependence are presented in Figure 17. As can be seen, the single scattering model presented above makes a very good description of the experimental data. Figure 18a shows the line width Ω of the power spectrum for polystyrene microsphere aqueous suspensions with various volume fractions (ρ) and three particle dimensions, as indicated. Remarkably, for the whole concentration interval, the results are within 4% of error with respect to the values calculated with Mie theory, which are represented by the solid lines. The independence of power spectrum line width on the volume fraction undoubtedly proves that the single-scattering description given by equation (43) is correct and that our technique can be used for dynamic systems over a broad range of concentrations. Dynamic light scattering in localized coherence volumes should find important applications for characterizing sub-diffusive or inhomogeneous scattering systems, where dynamic light scattering with coherent light cannot be applied. Due to (i) the inherent high dynamic range of the heterodyne detection, (ii) the efficient operation in single-mode optical fibers, and (iii) the effective isolation of the measurement volume, the technique presented here allows for a simultaneous determination of both particle size and concentration.

Figure 18b shows the measured values of the power spectrum amplitude A_0 for all the samples. As can be seen that A_0 depends linearly on the volume fraction ρ for all the particle dimensions. Moreover, the slope of the linear dependent is a function of the particle diameter, as shown in the logarithmic plot of Figure 18b. The curves have been further normalized by Q_b/d for each particle dimension and, as a result, all the experimental dependences collapsed into a single curve, as indicated by the inset of Figure 18b. This remarkable result permits to find

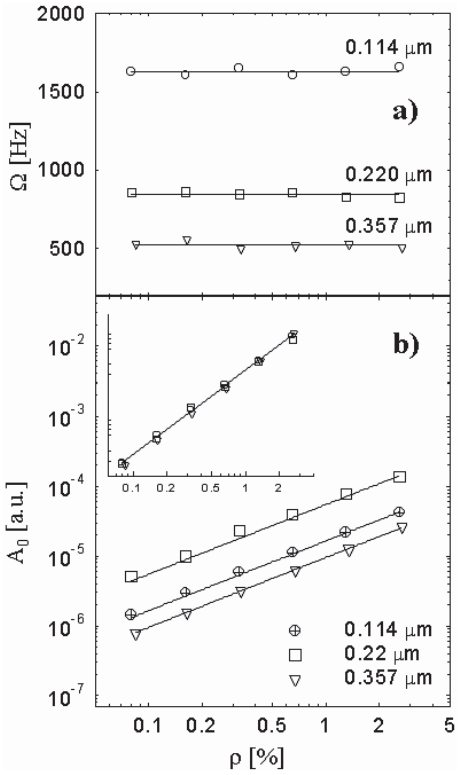

Fig. 18. Power spectrum line width (a) and amplitude (b) as a function of volume fraction, for colloidal suspensions of different particle sizes, as indicated. The inset of (b) shows the curves $A_0(\rho)$ collapsing into a unique dependence, after the normalization with Q_b/d.

the experimental constant α, which, in turn, gives access to the information regarding the particle concentration. Alternatively, for a medium with known density, the additional information contained in the spectrum amplitude provides the backscattering efficiency Q_b, which can be further related to the optical properties of the particles.

5.2 Microrheology using LCI

Soft materials, which include polymer solutions, surfactant solutions, and biological materials, among others, are characterized by complex structures with multiple characteristic time and length scales; as a consequence, their response to external strains has a non-trivial time dependence. One of the most important descriptors of these properties is the complex shear modulus $G(t)$, which is typically measured in the frequency domain ω. The real part $G'(\omega)$ in the frequency domain describes the elastic (storage) property of the system, while the imaginary part $G''(\omega)$ is a measure of the viscous (loss) behavior. The ability to measure locally how a material responds to an applied shear strain has a variety of applications, especially in biology, where the mechanical properties of the cells and intracellular matter are of utmost importance.

Recently a number of techniques have been developed or suggested for probing the rheological properties of

complex materials at a microscopic scale [56] – an area that has come to be known as *microrheology*. Most of the microrheological techniques rely on applying a strain to the fluid through embedded 'probe' particles, and the strains result either from the (Brownian) thermal noise imparted through the probe or from a suitable, externally imposed force on the probe. Microrheological measurements have been reported in the last few years for a number of materials, e.g., colloidal dispersions, polymer solutions, and biological cells and materials. For example, numerous experiments on acting networks have shown non-trivial high-frequency dependence of the shear modulus and models have been proposed to explain such behavior [57–61]. It is commonly agreed that most of the viscoelastic fluids have shear moduli that follow a power law dependence in the high-frequency region, but the actual value of the exponent appears to vary depending on the materials and, sometimes, the experimental technique used. Therefore, it is of great interest to find complementary investigation methods for high-frequency viscoelastic behavior of complex fluids at microscopic scales.

5.2.1 Principle of the technique

Using the principle of dynamic light scattering in localized coherence volumes presented earlier, we will describe a technique that relies on quantifying the motion of thermal particles embedded in the fluid under investigation [65]. Combining the properties of partially coherent light that is guided through a single-mode optical fiber, one can extract, from the intensity of the scattered light, the high-frequency limit of the power spectral density of the mean-squared displacements $\langle \Delta r^2(\omega) \rangle$ of the embedded, probe particles. The measurement volume becomes of the order of a tenth of a picoliter, which is about 5 to 6 orders of magnitude smaller than the one needed, for instance, in DWS-based techniques. The microrheological information is then obtained using the fluctuation-dissipation theorem that relates $\langle \Delta r^2(\omega) \rangle$ with the loss response $\chi''(\omega)$ that characterizes the fluid through

$$\chi''(\omega) = \frac{\omega}{2k_B T} \cdot \langle \Delta r^2(\omega) \rangle \,, \tag{46}$$

where k_B is Boltzmann's constant, and T is the absolute temperature of the material. Due to causality, the storage (memory) component $\chi'(\omega)$ and loss (dissipative) component $\chi''(\omega)$ of the response function $\chi(\omega)$ are related through the Kramers-Kronig equation:

$$\chi'(\omega) = \frac{2}{\pi} \mathcal{P} \int_0^\infty \chi''(\xi) \frac{\xi}{\xi^2 - \omega^2} d\xi, \tag{47}$$

where $\mathcal{P}$ indicates the principal value integral. The causality principle is often used in optics when one relates the real and the imaginary parts of the electric susceptibility. Thus, in spectroscopic applications, it is common to infer the spectral dependence of the refractive index of a material from the spectral characteristics of absorption, using a Kramers-Kronig relationship.

The main characteristic of this dynamic light scattering scheme is that the properties of the system under investigation are probed locally, which can reveal detailed information about its morphology. In addition, the use of an optical fiber allows a high degree of experimental flexibility, thereby enhancing the range of applicability of the technique. It is also important to emphasize another significant advantage offered by the elimination of multiple scattering effects in the proposed technique. The analysis of multiple scattering in DWS-based microrheological studies is based on the assumption that the photon path length is Gaussian. In systems in which the scatterers (either naturally present scatterers or embedded probe particles) are *not* in large enough concentration to justify the Gaussian assumption, DWS-based analyses of the data introduce numerical artifacts in the extracted complex moduli. Such artifacts, when not accounted for in the analysis of the data, are attributed to the frequency-dependence of the material properties of the fluid. In contrast, the low-coherence technique described before eliminates the multiple scattering effects so that the extracted modulus reflects the true property of the material.

In the following we will show how the local loss and elastic response of a complex fluid can be extracted from the response of the fluid to the thermal excitation communicated by the probe particles. The experimental setup is similar to the one described in Section 5.1. The intensity fluctuations are detected only from the coherence volume that is defined by the coherence length and the transversal dimension of the fiber core, in which the optical fields preserve relative phase correlations. The sensitivity of the technique is enhanced due to several reasons. First, the backscattered intensity is a product of the field amplitude of the scattered light and that of the Fresnel reflection. Therefore, the specular reflection amplifies the backscattering signal, as noted in the text. In addition, as in any heterodyne technique, the dynamic range is increased since the measured intensity is proportional to the squared root of the backscattered intensity and not to the intensity itself. Secondly, although the incident beam undergoes only single scattering due to the reduced dimensions of the coherence volume, the total detected signal is the result of backscattering from a collection of particles. Lastly, because the measurements are made directly in the frequency domain, the electrical noise is reduced dramatically by narrowing the bandwidth of the measurement and by extensive averaging.

The relationship between the normalized intensity and amplitude autocorrelation function has been shown in the previous chapter to have the form:

$$g^{(2)}(\tau) = 1 + \gamma g^{(1)}(\tau) \,, \tag{48}$$

where $\gamma = 2 I_0 I_s^{CV} \left(I_0 + I_s^{CV} \right)^2$, with I_0 and I_s^{CV} the total average intensities associated with the Fresnel component and the scattered light from the coherence volume (superscript "CV"), respectively. In all the experiments, the photon mean free path in the medium was always much longer than the coherence length of the light used. Thus, within the coherence volume, the single scattering regime

applies and the first-order autocorrelation function $g^{(1)}(\tau)$ can be written as

$$g^{(1)}(\tau) = \exp\left[-\frac{1}{6}q^2\left\langle \Delta r^2(\tau)\right\rangle\right], \tag{49}$$

where $q = 4\pi/\lambda$ is the magnitude of the scattering vector associated with our backscattering geometry, and $\left\langle \Delta r^2(\tau)\right\rangle$ is the mean-squared displacement of the particles under thermal motion. The quantity measured in the experiment is the power spectrum of the scattered light fluctuations $P(\omega)$, which is the Fourier counterpart of $g^{(2)}(\tau)$. At this point, we make the observation that, in the high-frequency region, $P(\omega)$ is directly related to the power spectral density of the particle displacements $\left\langle \Delta r^2(\omega)\right\rangle$ through

$$P(\omega) = \frac{\gamma q^2}{6}\left\langle \Delta r^2(\omega)\right\rangle. \tag{50}$$

Equation (50) holds true for times of evolution much shorter that the characteristic decaying time of the autocorrelation function, when equation (38) can be linearized as $g^{(1)}(\tau) = 1 - q^2\left\langle \Delta r^2(\tau)\right\rangle/6$. This approximation is similar to the first cumulant expansion used in deriving the Laplace relationship between the autocorrelation function and the pathlength probability distribution in the context of DWS [58]. With this approximation, it becomes apparent that the high-frequency dependence of the shear modulus $G(\omega)$ can be obtained by combining equations (45–46) using the relationship between the response function $\chi(\omega)$ and $G(\omega)$:

$$G(\omega) = \frac{1}{6\pi a}\frac{1}{\chi(\omega)}, \tag{51}$$

where a is the radius of the probe particles. Equation (51) is often referred to as the *generalized Stokes-Einstein equation*, and it is valid only under restricted conditions.

5.2.2 Investigation of purely viscous fluids

We will first illustrate the application of LCI microrheology on simple (i.e., purely viscous) fluids. For this, solutions of ethylene glycol (EG) in water at various concentrations were mixed with polystyrene microspheres of diameter 0.1 μm and 0.2 μm, at a volume fraction of 10^{-2}, as probe particles. The bandwidth of the measurement was 2 Hz, and each power spectrum was averaged typically over 100 measurements in order to increase the signal-to-noise ratio. The high-frequency (tail) regions of the power spectra were found to exhibit a power-law dependence of the form ω^{β}, and a least-square analysis of the data with this functional form led to $\beta = -2 \pm 0.01$ for all the EG solutions and water. Note that this result is what one would expect for the power spectra associated with purely viscous fluids at large frequencies, i.e., for viscous fluids $P(\omega)$ should have a Lorentzian shape, which, for high frequencies, implies a ω^{-2}-dependence. In order to compute the real and imaginary parts of the response function, we used the functional forms obtained from the fit over the frequency domain where they describe the experimental results accurately. This result, in combination with equations (46, 50), leads directly to $\chi''(\omega)$, from which one then obtains the memory component $\chi'(\omega)$ using the Kramers-Kronig relation, equation (47).

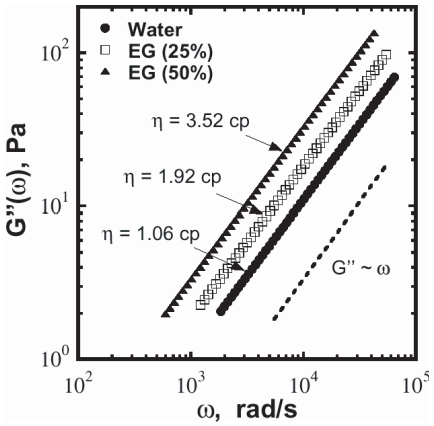

Fig. 19. Loss moduli for water and aqueous solutions of ethylene glycol (EG) at two different concentrations, as indicated. The dashed line indicates the ω^1 behavior. The viscosity ρ obtained from the fit is shown for each data set. The corresponding viscosities obtained using a mechanical viscometer are: $\eta = 1.02$, 2.01, and 3.9 for water and ethylene glycol solutions of concentrations 25% (vol.) and 50% (vol.), respectively.

In order to perform the Kramers-Kronig integration in equation (47), the power-law dependence of $P(\omega)$ on frequency has been assumed to be valid beyond the actual frequency interval measured. This is a common procedure necessary to avoid the effects of a limited bandwidth. The value of the integral was evaluated for points within the measurement interval. The results obtained are shown in terms of the loss modulus $G''(\omega)$ in Figure 19, for water and EG solutions at two different concentrations. The results shown are for probe particles of diameter 0.2 μm. A comparison of the results with the line of unit slope shown on the figure demonstrates the linear dependence of $G''(\omega)$ in all cases, consistent with what is expected for purely viscous fluids. The intercepts of linear fits of the data give the viscosities of the fluids and are also indicated in Figure 19. The results obtained ($\eta = 1.06, 1.92$, and 3.56 centipoise for pure water and EG concentrations of 25% and 50% by volume, respectively) are within 10% of values measured independently using a mechanical viscometer ($\eta = 1.02, 2.01$, and 3.9 centipoise, respectively). The corresponding storage moduli $G'(\omega)$ are essentially zero, as one would expect for purely viscous materials, and are not shown in the figure.

It is worth noting that the lower limit of the frequencies accessible in the experiments is determined by the frequency at which the experimental power spectrum deviates significantly from the power law behavior. The upper

limit of the frequency interval is set by the measurement noise and does not represent a limitation of the method itself, as the range could be extended with improved instrumentation and noise reduction. In all the experiments, we could obtain the shear modulus over a typical range of at least two orders of magnitude in frequency.

5.2.3 Viscoelasticity in localized volumes

We will now illustrate the use of the LCI technique for measuring the local response of viscoelastic materials such as polyethylene oxide (PEO) solutions of various concentrations and molecular weights. PEO is a water-soluble polymer available in a range of molecular weights (e.g., 10^3–10^7), and its local viscoelastic properties in concentrated solutions have been investigated previously [42]. Figure 20 shows two examples of raw power spectra $P(\omega)$ for aqueous solutions of PEO with an average molecular weight of 3×10^6 (denoted by PEO-3M, where the suffix 3M, for 3 million, identifies the molecular weight) at concentrations of 0.125% and 1.0% by weight, as indicated. As evident from Figure 20, the functional dependence of the measured power spectrum changes from a power of -1.91 (0.125 %) to -1.66 (1%) for large frequencies, indicating deviations from the response of a purely viscous fluid (for which one expects a Lorentzian for $P(\omega)$, corresponding to a ω^{-2} behavior at large frequencies, as discussed in the previous section). The above power spectra are converted to $G'(\omega)$ and $G''(\omega)$ as discussed in the previous section and the results are plotted in Figure 21. First, one notes that the relative behavior of $G''(\omega)$ and $G'(\omega)$ is consistent with what one would expect. In particular, the elastic component is much smaller than the loss modulus for the 0.125%-solution relative to the case of the 1%-solution, since the lower polymer concentration only marginally perturbs the essentially viscous behavior of the solution. Correspondingly, the slope of the loss modulus $G''(\omega)$ with respect to the frequency ω is about 0.91 – a small deviation from a slope of unity expected for purely viscous behavior. For the larger concentration, $G'(\omega)$ is noticeably larger than the one for the lower concentration, indicating stronger elasticity. One also notices that the corresponding $G''(\omega)$ increases more slowly with ω (as $\sim \omega^{0.66}$) than for the lower concentration.

In general, the ratio $G''/G' = \tan\delta$, known as the *loss tangent*, provides a measure of the material fluidity of viscoelastic fluids. The real and imaginary parts of $G(\omega)$ for each solution appear to have almost identical dependence on frequency, as suggested by the results shown in Figure 21; therefore, the loss tangent has a weak dependence on frequency for both concentrations in the range of frequency shown. However, the magnitude of the loss tangent does decrease considerably with polymer concentration, as expected. In general, the loss tangent should approach infinity for a purely viscous material such as water and decrease to zero as the system tends to a perfectly elastic material, such as a gel.

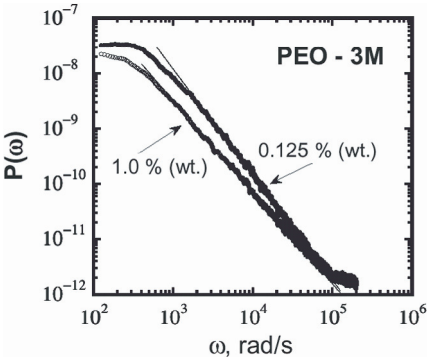

Fig. 20. The raw power spectra for PEO-3M solutions of two different concentrations (0.125% and 1% by weight) obtained using 0.2 μm particles.

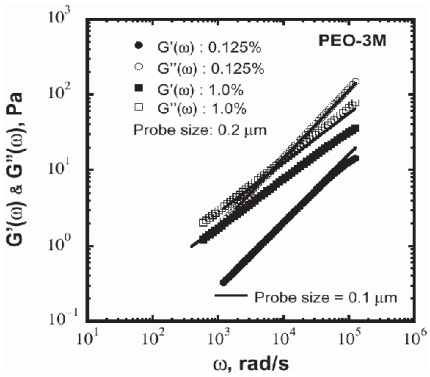

Fig. 21. The storage modulus G' and the loss modulus G'' for PEO-3M solutions at two different concentrations obtained using 0.2 μm particles. The results obtained with 0.1 μm on the same samples are represented by the solid lines.

5.2.4 Microrheology at interfaces of complex systems

A remarkable capability of the LCI technique is the possibility of probing changes in viscoelasticity *through* an interface as a function of spatial position *within* the interface. So far, we have demonstrated the ability to measure the rheological properties of complex fluids within small coherence volumes, and it has been shown that detailed information about the liquid-gel transition can be obtained with the approach proposed. The information about the fluid under investigation is retrieved from a measurement volume of the order of a tenth of a picoliter. This unique feature of our technique makes the method appealing for investigating systems with heterogeneities existing on a much smaller scale than could be measured with any other method. To illustrate this, we considered a test system with a gradient in the constitutive properties along one spatial coordinate, created by placing two different solutions in contact so that an interfacial region of about 2000 μm is formed. More specifically, an aqueous solution of ethylene glycol (25% by volume) was placed in contact with a polymer solution of PEO-8M (0.5% by mass) in a capillary tube of 1 mm diameter. The optical fiber (125 μm diameter) was then immersed in the liquid and successive measurements were taken at various depths, along the

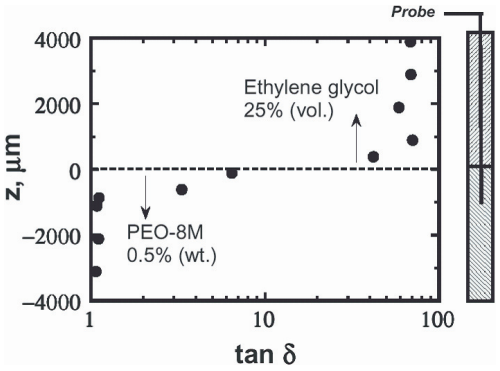

Fig. 22. Loss tangent as a function z-coordinate, as the optical fiber goes from a layer of simple viscous liquid [25% (vol.) of ethylene glycol] to a viscoelastic fluid [0.5% (wt.) of PEO-8M].

spatial concentration gradient created. The results for the loss tangent as a function of depth z are summarized in Figure 22. The figure demonstrates that there is a clear transition from a region of high loss tangent values associated with the viscous liquid (the ethylene glycol solution) to the low values characteristic of viscoelastic fluids (PEO-8M); the transition occurs over a distance of about 2000 μm. It can be seen that at the two extreme ends (above and below the interface), the values of the loss tangent show almost no dependence on z, thereby identifying homogeneity at the two extremes. The corresponding values of the loss tangent are in excellent agreement with the ones measured for each fluid independently. This remarkable result proves that the optical fiber slips through the fluid, without substantially carrying solute molecules from one solution to the other. A full three-dimensional mapping of the microrheological properties in highly heterogeneous complex fluids can be obtained thereby opening a new class of potential applications.

6 Summary

Light scattering is the method of choice for numerous sensing procedures. In this article, we have reviewed recent advancements in using low-coherence radiation for determining properties of various scattering media.

Starting from the characteristics of light scattering by individual particles, we have discussed the particularities of different scattering regimes Most interesting situations of practical interest are such that the light propagation is subject to scattering at many different locations within the probed volume. For a long time, the intensity and phase fluctuations which are determined by multiple light scattering were regarded as optical noise that degrades the radiation's properties. Several remarkable advances in experimental methodologies using broadband radiation proved that techniques based on multiple light scattering offer unprecedented capabilities. In particular, we have shown here that by adjusting the coherence properties of light, one can use interferometric approaches to select specific orders of scattering. As a result, spatial and temporal characteristics of optically inhomogeneous media could be determined in regimes of light-matter interaction ranging from single scattering to strong multiple scattering.

Based on the use of optical fibers, several sensing techniques have been described and their capabilities have been discussed in the context of characterizing the structural properties of static and dynamic scattering media. For instance, the physical properties of colloidal systems or porous media were determined noninvasively using optical procedures which rely on the properties of broadband radiation. Notably, the use of coherence gating has also been successfully used to determine the rheological properties of soft materials within picoliter volumes. Developments in light sources with adjustable coherence properties and advances in integrating optical devices will nevertheless offer more and more possibilities for developing fast and reliable sensing technologies based on optical scattering.

References

1. M. Kerker, *The Scattering of Light* (Academic Press, New York, 1969)
2. A. Ishimaru, *Wave propagation and Scattering in Random Media* (Oxford University Press, Oxford, 1997)
3. J.B. Keller, J. Opt. Soc. Am. **59**, 1003 (1969)
4. B. Cairns, E. Wolf, Opt. Commun. **74**, 284 (1990)
5. T.M. Habashy, R.W. Groom, B.R. Spies, J. Geophys. Res. **98**, 1759 (1993)
6. M. Born, E. Wolf, *Principles of Optics* (Cambridge University Press, Cambridge, 1999)
7. J.M. Ziman, *Models of Disorder* (Cambridge University Press, Cambridge, 1979)
8. N.E. Cusack, *The Physics of Structurally Disordered Matter* (Adam Hilger, Bristol, 1987)
9. For a review see E. Wolf, D.F.V. James, Rep. Prog. Phys. **59**, 771 (1996)
10. A. Dogariu, E. Wolf, Opt. Lett. **23**, 1340 (1998)
11. J.J. Duderstadt, L.J. Hamilton, *Nuclear Reactor Analysis* (Wiley, New York, 1976)
12. L. Mandel, E. Wolf, Rev. Mod. Phys. **37**, 2 (1965)
13. T. Shirafuji, H. Motomura, K. Tachibana, J. Phys. D **37**, R49 (2004)
14. R.C. Youngquist, S. Carr, D.E. Davies, Opt. Lett. **12**, 158 (1987)
15. D. Huang, E.A. Swanson, C.P. Lin, J.S. Schuman, W.G. Stinson, W. Chang, M.R. Hee, T. Flotte, K. Gregory, C.A. Puliafito, J.G. Fujimoto, Science **254**, 1178 (1991)
16. A.F. Fercher, W. Drexler, C.K. Hitzenberger, T. Lasser, Rep. Prog. Phys. **66**, 239 (2003)
17. A.F. Fercher, C.K. Hitzenberger, G. Kamp, S.Y. El-Zaiat, Opt. Comm. **117**, 43 (1995)
18. C. Mujat, A. Dogariu, Opt. Exp. **12**, 1335 (2004)
19. U. Morgner, W. Drexler, F.X. Kartner, X.D. Li, C. Pitris, E.P. Ippen, J.G. Fujimoto, Opt. Lett. **25**, 111 (2000)
20. C. Yang et al., Opt. Lett. **25**, 1526 (2000)
21. C. Yang et al., Opt. Lett. **26**, 1271 (2001)
22. H. Iwai et al., Opt. Lett. **29**, 2399 (2004)
23. G. Popescu et al., Opt. Lett. **29**, 2503 (2004)
24. T. Ikeda, G. Popescu, R.R. Dasari, M.S. Feld, Opt. Lett. **30**, 1165 (2005)
25. G. Popescu, A. Dogariu, Appl. Optics **39**, 4469 (2000)
26. G. Zaccanti, P. Bruscaglioni, J. Mod. Opt. **35**, 229 (1988)

27. W.G. Tam, A. Zardecki, Appl. Optics **21**, 2405 (1982)
28. M. Kempe, A.Z. Genack, W. Rudolph, P. Dorn, J. Opt. Soc. Am. **14**, 216 (1997)
29. G. Jarry, E. Steimer, V. Damaschini, M. Jurczak, R. Keiser, J. Opt. **28**, 83 (1997)
30. M.R. Hee, J.A. Izatt, J.M. Jacobson, J.G. Fujimoto, Opt. Lett. **18**, 1107 (1993)
31. M.R. Hee, J.A. Izatt, E.A. Swanson, J.G. Fujimoto, Opt. Lett. **18**, 950 (1993)
32. B.B. Das, K.M. Yoo, R.R. Alfano, Opt. Lett. **18**, 1092 (1993)
33. S.G. Demos, R.R. Alfano, Opt. Lett. **21**, 161 (1996)
34. A. Dogariu, I. Uozumi, T. Asakura, Ballistic Propagation of Light Through Fractal Gels, Wave In Random Media **4**, 1 (1994)
35. G. Popescu, A. Dogariu, Opt. Lett. **24**, 442 (1999)
36. C. Mujat, L. Denney, A. Dogariu, Mat. Res. Soc. Symp. Proc. **613**, E.6.10.1 (2000)
37. C. Mujat, M. van der Veen, J.L. Rueben, J. Ten Bosch, A. Dogariu, Appl. Opt. **42**, 2979 (2003)
38. G. Popescu, C. Mujat, A. Dogariu, Phys. Rev. E **61**, 4523 (2000)
39. B.J. Berne, R. Pecora, *Dynamic light scattering with applications to Chemistry, Biology, and Physics* (Wiley, New York, 1976)
40. G. Maret, P.E. Wolf, Z. Phys. B **65**, 409 (1987)
41. D.J. Pine, D.A. Weitz, P.M. Chaikin, E. Herbolzheimer, Phys. Rev. Lett. **60**, 1134 (1988)
42. T.G. Mason, H. Guang, D.A. Weitz, J. Opt. Am. A **14**, 139 (1997)
43. E.M. Furst, A.P. Gast, Phys. Rev. E **58**, 3372 (1998)
44. P. Hebraud, F. Lequeux, J.P. Munch, Phys. Rev. Lett. **78**, 4657 (1997)
45. T. Gisler, D.A. Weitz, Phys. Rev. Lett. **82**, 1606 (1999)
46. G. Nissato, P. Hebraud, J.-P. Munch, S.J. Candau, Phys. Rev. E **61**, 2879 (2000)
47. M.F. Clapper, J.S. Collura, D. Harrison, M.R. Fisch, Phys. Rev. E **59**, 3631 (1999)
48. R. Carminati, E. Elaloufi, J.-J. Greffet, Phys. Rev. Lett. **92**, 213903 (2004)
49. G. Popescu, A. Dogariu, Appl. Optics **40**, 4215 (2001)
50. P.A. Lemieux, M.U. Vera, D.J. Durian, Phys. Rev. E **57**, 4498 (1998)
51. D.J. Pine, D.A. Weitz, J.X. Zhu, E. Herbolzheimer, J. Phys. France **51**, 2101 (1990)
52. I. Flammer, J. Ricka, Appl. Opt. **36**, 7508 (1997)
53. T. Bellini, M.A. Glaser, N.A. Clark, Phys. Rev. A **44**, 5215 (1991)
54. K.K. Bizheva, A.M. Siegel, D.A. Boas, Phys. Rev. E **58**, 7664 (1998)
55. G. Popescu, A. Dogariu, Opt. Lett. **26**, 551 (2001)
56. F.C. MacKintosh, C.F. Schmidt, Curr. Opin. Colloid. In. **4**, 300 (1999)
57. F. Gittes, B. Schnurr, P.D. Olmsted, F.C. MacKintosh, C.F. Schmidt, Phys. Rev. Lett. **79**, 3286 (1997)
58. T.G. Mason, D.A. Weitz, Phys. Rev. Lett. **74**, 1250 (1995)
59. F. Gittes, F.C. MacKintosh, Phys. Rev. E **58**, R1241 (1998)
60. D.C. Morse, Phys. Rev. E **58**, R1237 (1998)
61. J. Xu, A. Palmer, D. Wirtz, Macromolecules **31**, 6486 (1998)
62. J.C. Crocker, M.T. Valentine, E.R. Weeks, T. Gisler, P.D. Kaplan, A.G. Yodh, D.A. Weitz, Phys. Rev. Lett. **85**, 888 (2000)
63. A.J. Levine, T.C. Lubensky, Phys. Rev. Lett. **85**, 1774 (2000)
64. A.J. Levine, T.C. Lubensky, Phys. Rev. E **65**, 011501 (2002)
65. G. Popescu, A. Dogariu, R. Rajagopalan, Phys. Rev. E **65**, 041504 (2002)

To access this journal online:
www.edpsciences.org